

THESIS FOR THE DEGREE OF LICENTIATE OF ENGINEERING

in

Thermo and Fluid Dynamics

CFD of Air Flow in Hydro Power Generators

by

Pirooz Moradnia

Department of Applied Mechanics
CHALMERS UNIVERSITY OF TECHNOLOGY
Göteborg, Sweden, 2010

CFD of Air Flow in Hydro Power Generators
Pirooz Moradnia

© PIROOZ MORADNIA, 2010

THESIS FOR LICENTIATE OF ENGINEERING no. 2010:11
ISSN 1652-8565

Department of Applied Mechanics
Chalmers University of Technology
SE-412 96 Göteborg
Sweden
Telephone +46-(0)31-7721000

This document was typeset using \LaTeX

Printed at Chalmers Reproservice
Göteborg, Sweden, 2010

CFD of Air Flow in Hydro Power Generators

PIROOZ MORADNIA

pirooz.moradnia@chalmers.se
Department of Applied Mechanics
Chalmers University of Technology

Abstract

The air flow through a generator has been numerically investigated with different rotor and stator designs to give a better understanding of the flow for cooling purposes. A simple rotor design has been chosen to start with, and modified through a set of changes, where stepwise modifications have been imposed to the design of the rotor and the stator. The flow properties for all cases have been compared to each other to see the effect of each parameter change on the flow inside the machine.

The flow is predicted with the OpenFOAM solver *MRFSimpleFOAM*, which uses the Frozen Rotor concept. This means that there is no actual mesh movement in this study, but instead, the rotating regions in the domain are provided with source terms that account for rotation.

The choice of the turbulence model for solving the air flow in the generator was based on a study of the turbulence models and validation test cases. All incompressible RAS turbulence models in OpenFOAM-1.5.x were studied and the implementations were compared to the original models. Many of the mentioned turbulence models were tested on a backward-facing step test case. The numerical results were compared to the experimental data and the most appropriate turbulence model was chosen. Details on turbulence model studies are discussed in Appendix A. A laminar Couette flow between two concentric cylinders was run and the numerical velocity and pressure distributions between the cylinders were compared to the analytical results. More details on the validation test cases are found in Appendix B.

Keywords: CFD, Generator, OpenFOAM, Launder-Sharma $k-\varepsilon$,MultipleReferenceFrame

List of Publications

This thesis is partly based on the work contained in the following paper:

I P. Moradnia and H. Nilsson, 2010, CFD of Air Flow in Hydro Power Generators for Convective Cooling, using OpenFOAM, *EC-COMAS 2010*, June 14-17, Lisbon, Portugal

Acknowledgments

The research presented in this thesis was carried out as a part of the "Swedish Hydropower Centre - SVC". SVC has been established by the Swedish Energy Agency, Elforsk and Svenska Kraftnät together with Luleå University of Technology, The Royal Institute of Technology, Chalmers University of Technology and Uppsala University. Participating hydro power companies are: Andritz Hydro, E.ON Vattenkraft Sverige, Fortum Generation, Holmen Energi, Jämtkraft, Karlstads Energi, Linde Energi, Mälarenergi, Skellefteå Kraft, Sollefteå-forsens, Statkraft Sverige, Statoil Lubricants, Sweco Infrastructure, Sweco Energuide, SveMin, Umeå Energi, Vattenfall Research and Development, Vattenfall Vattenkraft, VG Power and WSP.

The computer facilities were provided by Chalmers Center for Computational Science and Engineering (C^3SE) and the Swedish National Infrastructure for Computing (SNIC).

I would like to express my sincere gratitude to my supervisor, Håkan Nilsson, for all his precious guidance and continuous support. Many thanks for being patient and for helping me develop a broader and more precise sight.

I would also like to thank Tage Carlsson, Johan Westin, Daniel Rundström and Bo Hernnäs for the nice comments and fruitful discussions. Many thanks to Urban Lundin and Mattias Wallin for their time and for providing us with access to the SVANTE generator at Uppsala university, as well as modifying it to meet our needs.

Many thanks to my colleagues at the Division of Fluid Dynamics for the pleasant work environment and to my friends for their company and all nice moments together.

Finally and most importantly, I would like to thank my family for their endless and unconditional support. I know you are there for me, thanks for everything!

Nomenclature

Latin symbols

$C_{\varepsilon 1}$	constant in $k - \varepsilon$ turbulence model
$C_{\varepsilon 2}$	constant in $k - \varepsilon$ turbulence model
C_μ	constant in $k - \varepsilon$ turbulence model
D	extra source term in k equation of low-Re turbulence models
E	extra source term in ε equation of low-Re turbulence models
f_1	damping function in ε equation of low-Re turbulence models
f_2	damping function in ε equation of low-Re turbulence models
f_μ	damping function in ν_t formulation of low-Re turbulence models
k	turbulent kinetic energy
p	pressure
P_k	turbulent production term
q	\sqrt{k}
S_{ij}	strain rate tensor
u_*	friction velocity
$U_{i,j} \equiv \frac{\partial U_i}{\partial x_j}$	velocity derivative
u_i	Cartesian components of velocity vector
x_i	Cartesian coordinate vector component

Greek symbols

δ_{ij}	Kronecker delta
ε	dissipation of turbulent kinetic energy
$\kappa = 0.41$	von-Karman constant
μ	laminar dynamic viscosity
μ_t	dynamic turbulent viscosity
ν	kinematic viscosity
ν_t	kinematic turbulent viscosity
ω	specific dissipation, rotational speed of the rotor
ω_m	rotational speed of the reference frame
Ω_{ij}	rotation tensor
ρ	density
σ_k	constant in k-epsilon turbulence model

σ_ε constant in k-epsilon turbulence model
 τ_{ij} shear stress tensor
 ζ dissipation of q

Contents

Abstract	iii
List of Publications	v
Acknowledgments	vii
1 Introduction	1
2 Cases and Results	5
2.1 Cases	7
2.2 Volume Flow Distributions	9
2.3 Rotor Axial Power	11
2.4 Flow Structure	13
2.5 Flow in the Channels	15
2.6 Velocity Components Just Above the Rotor Poles	18
2.7 Relative Tangential Velocity in the Pole Gap	20
2.8 Pressure Distributions on the Rotor Poles	21
3 Concluding Remarks and Future Work	25
Appendices	27
A Modeling	29
A.1 Turbulence Models	29
A.1.1 Mathematical Notation in OpenFOAM	30
A.1.2 kEpsilon	32
A.1.3 RNGkEpsilon	32
A.1.4 realizableKE	33
A.1.5 kOmegaSST	34
A.1.6 NonlinearKEShah	36
A.1.7 LienCubicKE	37
A.1.8 QZeta	38
A.1.9 LaunderSharmaKE	39
A.1.10 LamBremhorstKE	40

A.1.11	LienLeschzinerLowRe	41
A.1.12	LienCubicKELowRe	42
A.1.13	LRR	43
A.1.14	LaunderGibsonRSTM	45
A.1.15	SpalartAllmaras	46
A.2	Wall Functions	47
A.2.1	Linear $k - \varepsilon$ Models	47
A.2.2	Non-linear $k - \varepsilon$ Models	48
A.2.3	The kOmegaSST Model	48
A.3	Numerical Methods	49
A.3.1	Central Differencing, CD	49
A.3.2	Upwind Differencing, UD	49
A.3.3	Gamma Differencing	50
A.4	Frozen Rotor	51
A.5	Forces and Torques on the Rotor	51
B	Test Cases and Validation	53
B.1	Turbulence Model Validation Test Case	53
B.2	Case specifications	54
B.3	Results	56
B.3.1	Normalized velocity profiles, U/U_{cl}	56
B.3.2	Turbulent kinetic energy, k	59
B.3.3	y^+ value	62
B.3.4	Wall Shear Stress, τ_{wall}	64
B.3.5	Choice of Turbulence Model for the Generator	67
B.4	Concentric Cylinders	67
Bibliography		69
Paper I		

Chapter 1

Introduction

ALMOST half of the total electric power generation in Sweden comes from the hydroelectric power plants. Obviously any modifications and improvements to these systems would lead to considerable contributions to the total electric energy produced in the country. As any other complicated system, a hydroelectric power plant comprises a large number of different components, any of which should be carefully designed and optimized with respect to the working conditions to yield the highest possible efficiency at the normal working conditions.

In this work, the focus is on electric generators and the cooling air flow within them. A generator is a device which generates electricity through magnetic induction into its coils. The generator is made up of two main components: a rotor and a stator. The rotor is the rotating part of the generator, which holds a number of large electromagnetic poles. The stator is the stationary part, which is composed of a large number of electric conductors, called windings. When the rotor rotates, the motion of its magnetic field induces an alternating electric current in the stator windings. A transformer is then used to increase the voltage which leads to a decreased current with the same power, ($Power = Voltage \times Current$). The electricity is then transmitted to the network.

The process of conversion of the mechanical energy into electricity includes losses due to

- 1) Electrical resistance in the generator components, which comes up when there is an electric current passing through a resistance.
- 2) Magnetic field, which exerts force on the magnetic particles in the generator and causes molecular friction.
- 3) Mechanical losses, due to ventilation of the generator and friction between different parts.

The losses rise the temperature of the components, which leads to a change in the material properties. This includes electric resistances

and conductivities, which are temperature dependent. A working temperature beyond the prescribed values may result in deteriorated performance and lower efficiency of the generator in converting the energy to electricity. Also, the material strengths of certain components, such as insulations, are affected by temperature, causing a reduction in life time. All this means that the heat generated by the energy conversion process in the generators should be removed in order to keep the machine near its best operational point. Usually the heat in a generator is removed by means of convection. A number of cooling channels are provided in the stator body to allow for the passage of air to cool down the stator windings. The rotor acts as a fan, which builds up a pressure difference that pushes the air through the stator channels. Figure 1.1 shows the different parts of an axially cooled generator. In an axially cooled generator, the air flows axially into the machine and passes through the space between the rotor poles and into the stator channels. The stator channels are extended radially through the stator.

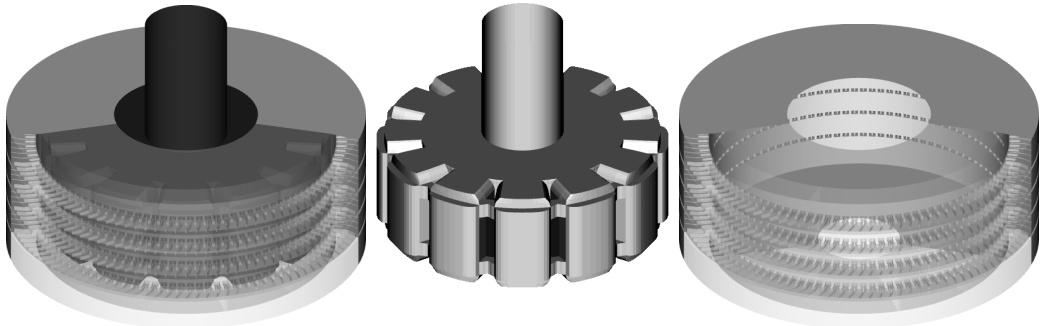


Figure 1.1: The simplified generator geometry used in the present work. **Left:** the complete model. **Center:** the rotor. **Right:** the stator. Transparency has been used to visualize the interior of the geometry.

The aim of this work is to numerically study the air flow in an axially cooled generator. Heat transfer is not included in the present study. The focus is instead on different geometrical attributes of the generator, and its effect on the flow distribution. There is also a focus on the choice of numerical methods and model, which is necessary before including the heat transfer.

In this report, first the different generator configurations are described and the numerical results for the cases are presented. Then the conclusions are drawn and future work is discussed. In Appendix A modeling methods are discussed. The Discussions concern different incompressible RAS turbulence models, wall treatment methods and a number of numerical methods in OpenFOAM OpenFOAM-1.5.x as well as the Frozen Rotor concept and methods for computing forces and

CHAPTER 1. INTRODUCTION

torques on the rotor. In Appendix B the validation test cases, the backward facing step and the Couette flow, are presented and discussed.

Chapter 2

Cases and Results

As Figure 1.1 shows, the rotor in the present study has 12 poles. The stator body contains a number of air passages, called stator channels, which allow for the flow of the cooling air through the generator. The stator channels are separated in the tangential direction by small baffles, which are used as supports to separate the stator plates. A stator winding passes through each channel between the baffles. The stator channels are shown in Figure 2.1. The channels are provided in 4 axial rows. Each row contains 108 channels. With 108 stator channels in each row, each pole can be associated with 9 channels in the circumferential direction. Thus, one can simplify the problem by modeling only 1 pole with 9 corresponding channels in each row, i.e. only a 1/12 sector with periodic boundaries. Also, since the geometry is axially symmetric, the computational domain can be further reduced by considering only the upper part and utilizing a symmetry boundary condition at the symmetry plane.

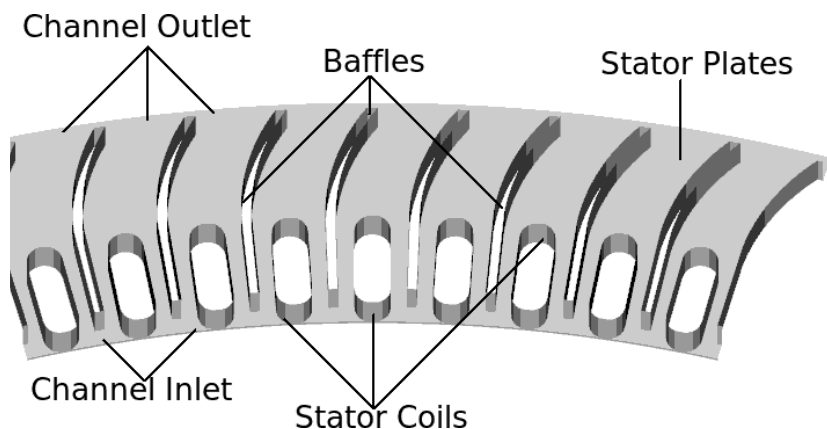


Figure 2.1: A close-up view of the stator channels

Figure 2.2 shows the computational domain by visualizing all the boundaries except the periodic boundaries of one of the studied cases, and a cross-section of the pole and the nine stator channels with their coils and baffles.

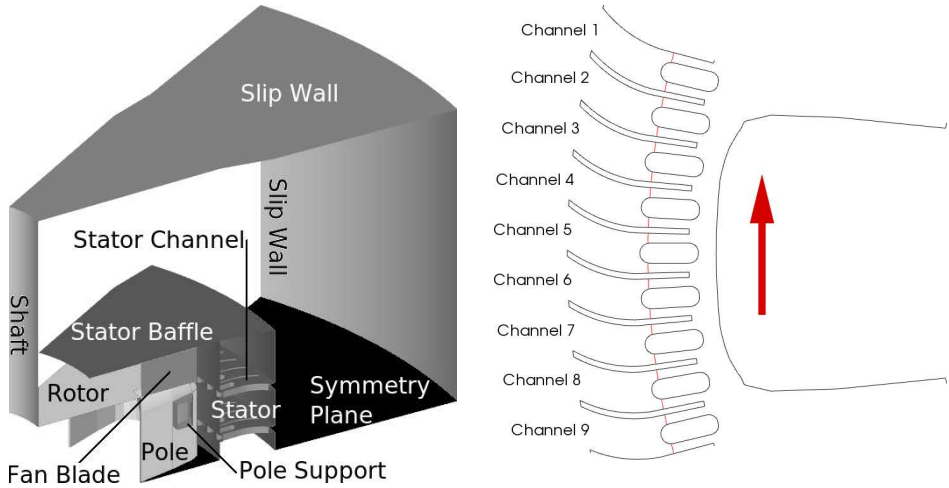


Figure 2.2: Left: Computational domain of a case where the 1/12 periodic sector and symmetry plane can be seen. The front and back boundaries (not shown) are periodic. **Right:** Rotor pole and stator cooling channels. The rotor is moving clockwise when seen from above

The flow is driven by the pressure build-up caused by the rotation of the rotor and interaction of the air flow with the rotor and the stator walls. Noticing the movement of the rotor relative to the stator, the flow should be pulsating and unsteady. In the present work, however, the simulations have been performed using the steady-state Frozen Rotor concept. In the Frozen Rotor concept the computational domain and the corresponding mesh are not rotating, but instead source terms for the rotation have been added to the governing equations in the rotating region. This is described in detail in the Appendix A.

The computational domain is generated without inlets and outlets. The reason for this choice is discussed in the following sections. It is, thus, the rotation of the rotor which drives the flow and, therefore, the volume flow through the machine is determined by the solution, rather than by a prescribed value at the inlet.

The turbulence is modeled utilizing the low-Re Launder sharma turbulence model. The use of a low-Re turbulence model is justified by the relatively small Reynolds number in the stator channels. It is beneficial with a fine mesh to capture the sharp gradients, especially in the near-wall regions where the modeled wall shear stresses are quite sensitive to the mesh quality. A high-Re turbulence model would lead

to a mesh that is too coarse to resolve many of the flow features. This is described in more details in Appendix A.

2.1 Cases

The geometry is a simplified version of a small generator at Uppsala University in Sweden. A simple pole design was selected and then modified in several steps to resemble the real geometry at the end. The generator cases include modifications to the rotor pole and the stator. There are 7 different rotor pole designs. Each pole design is assigned a number (from 1 to 7). Except for the pole design 1, each pole design is based on the previous pole design with geometric modifications. Table 2.1 shows the pole designs and the respective modifications to them.

Pole design	Remarks and Modifications
1	Base pole geometry with radial pole sides
2	Reduced areas A_1 and A_2 and non-radial sides
3	Added wedge shaped pole supports in between the poles
4	Curved front part of the poles
5	Curved edges on top of the poles
6	More curvature on top of the poles
7	Flattened top-front part of the poles

Table 2.1: Different rotor pole designs and the respective modifications.

Every modified rotor geometry has been simulated with three different layouts: a base case ($C\#$ cases), a case with a baffle on top of the stator ($C\#S$ cases), and a case with a combination of a stator baffle and a rotor fan blade between the poles ($C\#F$ cases). In all cases the stator inner diameter is $0.365m$ and the rotor rotational speed is $500rpm$. A_1 is the cross-sectional area between the poles in the computational domain. A_2 is the cross-sectional area of the air gap between the rotor and the stator in the computational domain. Figure 2.3 shows the schematic views of A_1 and A_2 as the shaded areas between the rotor and stator.

A parametric study of the effect of different parts of the geometry on the flow has been performed. In every step the flow in the modified geometry was simulated to study the effect of the geometrical changes on the flow. Table 2.2 shows all the different cases that have been studied in the present work.

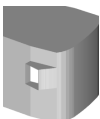
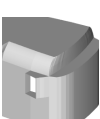
$C\#$	$C\#S$	$C\#F$	$A_1(m^2)$	$A_2(m^2)$	Pole modifications
C1	C1S	C1F	0.0033	0.0028	None 
C2	C2S	C2F	0.0029	0.0017	Sides, Radius 
C3	C3S	C3F	0.0029	0.0017	Pole supports 
C4	C4S	C4F	0.0029	0.0017	Curved front 
C5	C5S	C5F	0.0029	0.0017	Curved edges 
C6	C6S	C6F	0.0029	0.0017	More curved edges 
C7	C7S	C7F	0.0028	0.0017	Flattened top-front 

Table 2.2: Different rotor and stator designs. A_1 is the cross-sectional area between the poles in the computational domain, A_2 is the cross-sectional area of the air gap between the rotor and the stator in the computational domain.

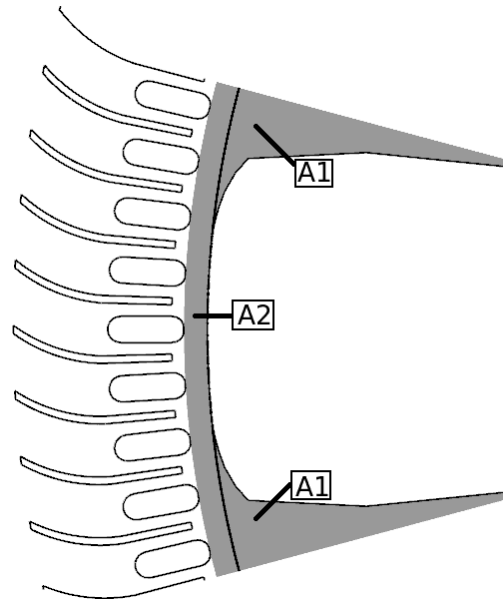


Figure 2.3: The schematic views of areas A_1 and A_2

2.2 Volume Flow Distributions

The distribution of volume flow between the channels are shown in Figure 2.4. The upper diagrams show the upper channel row, and the lower diagrams show the lower channel row. The vertical axis shows the volume flow of each channel. The horizontal axis shows the channel numbers, which are in accordance with the numbering shown in Figure 2.2, meaning that the rotor is rotating from channel 9 towards channel 1. The vertical dotted lines show the tangential position of the pole edges in relation to the stator channels.

As Figure 2.4 suggests, the use of a stator baffle above the rotor ($C \# S$) increases the volume flow through the machine. This is due to the higher pressure build-up inside the machine.

Generally, the addition of fan blades to the rotor increases the volume flow even more. This is however not true in the case $C7F$. That case shows unsteady characteristics and does not converge as easily as the other cases, and it thus needs further investigation. The increase in volume flow due to the inclusion of fan blades can again be justified by a higher pressure build-up in the generator. A larger pressure difference between the inside and the outside of the machine leads to a larger volume flow.

Figure 2.5 shows the relative distribution of the volume flow between the channels for all cases. The small rectangles show the channels in two rows and the large rectangle shows the pole edges. The

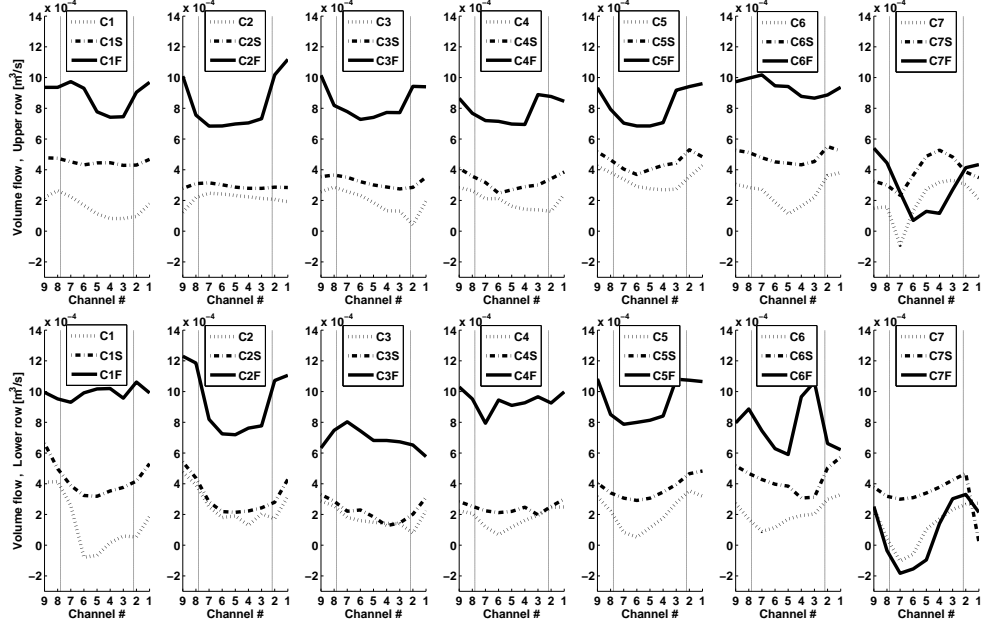


Figure 2.4: Distribution of the volume flows in the stator channels. Top: the upper row, bottom: the lower row. From left to right: C1, C2, C3, C4, C5, C6 and C7 variations. Channel numberings according to Figure 2.2

vertical axis shows the channel volume flow normalized with the total volume flow of each case. The zero- volume flow lines are shown by the horizontal dotted lines along the center of the channels. Notice that cases $C1$, $C7$ and $C7F$ have purely negative flows in some channels and also a more uneven distribution of volume flows.

Table 2.3 shows the rotor pole designs as well as the volume flow in the computational domain, and the average air flow velocity at the minimum cross sectional area of the stator channels. This local velocity is computed by dividing the volume flow through the computational domain by the minimum cross-sectional area of the stator channels. The minimum cross-sectional area of a single stator channel, near the stator coils, is $A_m \approx 8.29 \times 10^{-5} (m^2)$. It should be noted that each case has its own volume flow, \dot{V}_f , which is obtained by the solution. Since a total number of 18 stator channels are included in the computational domain, the velocity is given by

$$v_m = \frac{\dot{V}_f}{18 \times A_m}$$

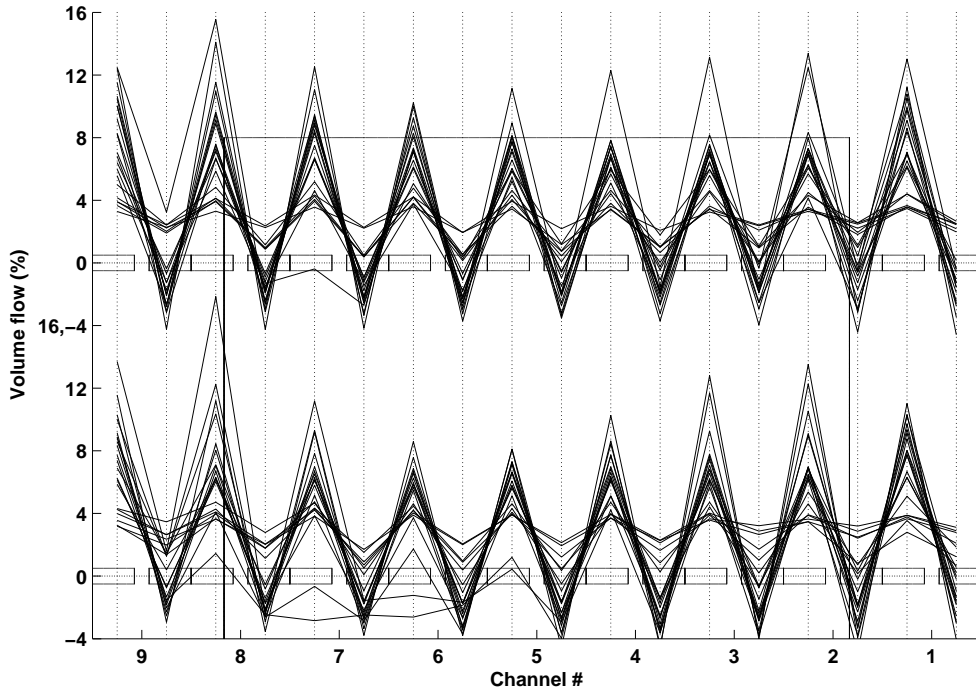


Figure 2.5: Relative volume flow distribution between all channels. Channel numbering according to Figure 2.2

2.3 Rotor Axial Power

Table 2.4 shows the axial power required to rotate the rotor. As described in Appendix A, the axial power of the rotor is divided into two parts: a part to overcome the moments from pressure forces, \dot{E}_p , and a part to overcome the moments from viscous forces, \dot{E}_v , i.e.

$$\dot{E}_{rotor} = \dot{E}_p + \dot{E}_v$$

As Table 2.4 suggests, the contribution from viscous forces is much smaller than that of the pressure forces. Large separation regions lead to large pressure drops on the rotor pole surfaces which exert large forces on the pole in the direction opposite to the motion of the rotor. The use of a stator baffle leads to a reduction in \dot{E}_p and generally a small reduction in \dot{E}_v . However, the values for \dot{E}_v are both small do not change significantly, which makes it difficult to draw conclusions about them. The use of fan blades strongly increases \dot{E}_p but still reduces \dot{E}_v (This does not apply to case C7F). The increase in \dot{E}_p with the use of fan blades can be justified by the larger volume flow through the generator. The amount of air flowing through the machine is larger and the fan

	C1	C2	C3	C4	C5	C6	C7	
C#	\dot{V}_f	0.0027	0.0042	0.0033	0.0034	0.0050	0.0041	0.0030
	v_m	1.8	2.8	2.2	2.3	3.4	2.7	2.0
C#S	\dot{V}_f	0.0079	0.0055	0.0049	0.0051	0.0074	0.0083	0.0069
	v_m	5.3	3.7	3.3	3.4	5.0	5.6	4.6
C#F	\dot{V}_f	0.0168	0.0158	0.0137	0.0155	0.0157	0.0154	0.0029
	v_m	11.3	10.1	9.2	10.4	10.5	10.3	2.0

Table 2.3: Rotor pole design, volume flow and average stator channel flow velocity. $\dot{V}_f(\frac{m^3}{s})$: The volume flow rate through the computational domain, $v_m(\frac{m}{s})$: Average velocity at the minimum channel cross-sectional area

	C1	C2	C3	C4	C5	C6	C7	
C#	\dot{E}_p	4.45	2.42	2.24	2.27	4.04	3.73	3.97
	\dot{E}_v	0.30	0.34	0.34	0.32	0.28	0.23	0.05
C#S	\dot{E}_p	3.62	2.29	1.94	1.98	2.82	3.25	3.27
	\dot{E}_v	0.25	0.31	0.28	0.28	0.26	0.26	0.04
C#F	\dot{E}_p	7.07	7.59	6.00	6.01	5.97	6.30	2.10
	\dot{E}_v	0.24	0.11	0.19	0.22	0.23	0.25	0.15

Table 2.4: Rotor axial power for all cases. $\dot{E}_p(W)$: The axial power required on the rotor to overcome the pressure moments. $\dot{E}_v(W)$: The axial power required on the rotor to overcome the frictional moments.

blades should give rotation to the flow, which means that more power is needed to rotate the rotor. Also, large separation areas behind the blades lead to a large pressure loss in those regions.

The reduction in \dot{E}_v can be justified by taking into account that using fan blades helps pushing more air in the desired direction within the machine. This means that the recirculations in the vicinity of the pole are minimized and, thus, friction between the air and the pole is also reduced. In case *C7F* a reduction in \dot{E}_p can be observed, which can be justified with the very low volume flow in the machine. At the same time, an increase in \dot{E}_v is noticed. This can be related to the frictional forces which are more intense in the backflow regions. A high relative velocity between the flowing air and the rotating pole leads to large frictional losses, without adding to the volume flow passing through the machine.

2.4 Flow Structure

The unit vectors of the velocity between the rotor poles (the cyclic boundaries in the computational domain, c.f. Figure 2.2) are shown in Table 2.5. The use of unit vectors makes the flow behaviour more clear in this case, where there is a large difference in velocity magnitudes. The contours of zero axial velocity are marked by thin curves.

Ideally, the velocity vectors should not point upwards in the computational domain (upper half of the generator). This means that the flow at the inlet to the machine should always be inwards and that all the fluid should flow directly through the channels. This way the air is heated up by the hot surfaces of the machine and removes the heat by flowing directly outwards. In reality this does not happen, since a number of flow recirculations will appear, based on the design of rotor and stator, as well as the rotational speed of the rotor. The recirculation of the cooling air in the machine causes the air to get warmer as it stays a longer time in contact with the hot surfaces, which reduces the temperature difference between the surfaces and the cooling air. This impairs the convective cooling of the machine.

In all cases, there is a region near the stator inner wall which has upward velocity vectors. This is not desirable according to the descriptions above. Also, it makes it difficult to define and use appropriate inlet boundary conditions (at the inlet to the machine) which can suit the flow characteristics. This justifies the use of stator baffles which prohibit the outward flow at the inlet to the machine. Obviously, adding a baffle on top of the rotor-stator space forces the velocity vectors to be directed downwards. This is based on the negative pressure gradients

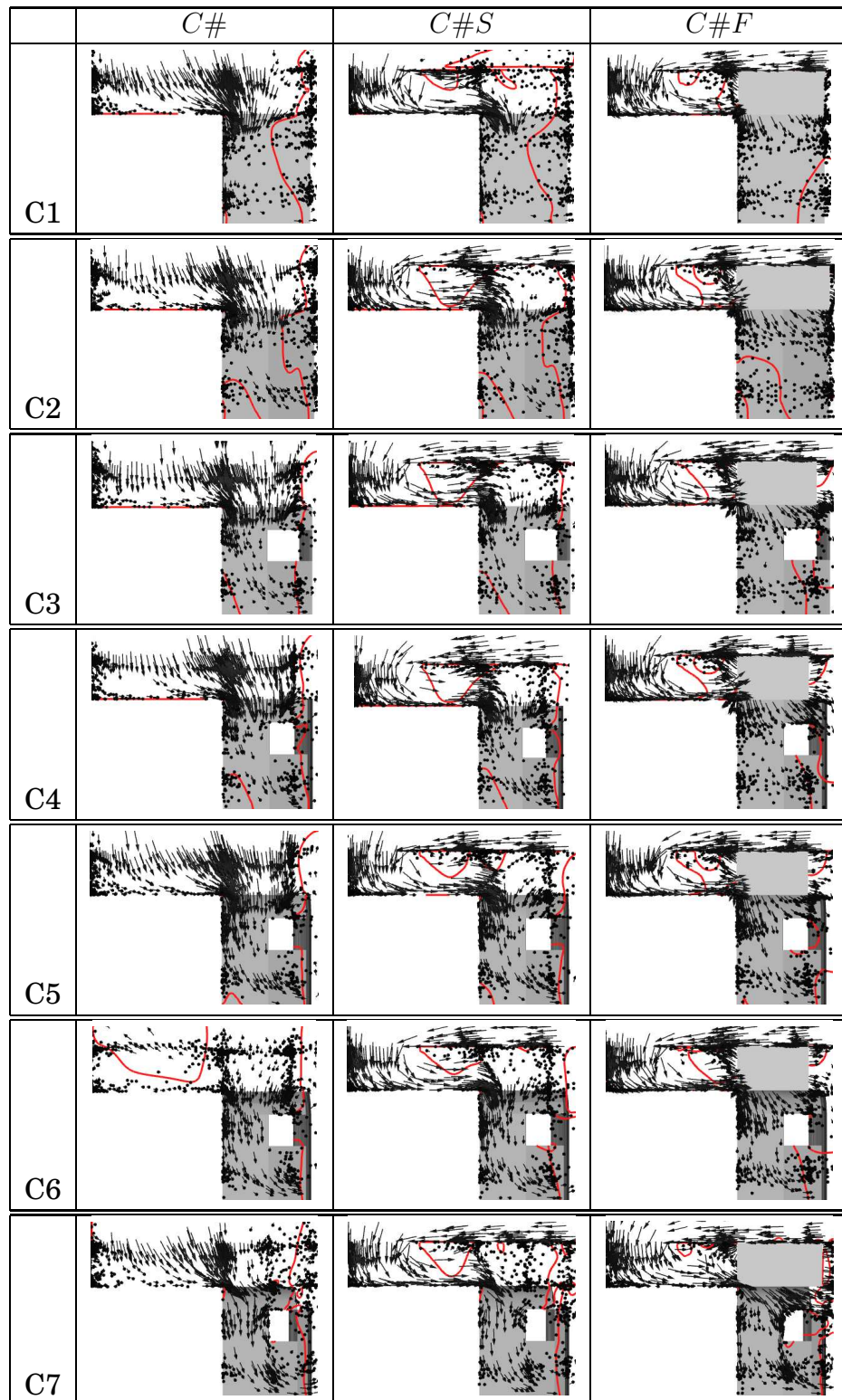


Table 2.5: Velocity unit vectors in a plane between two poles (the periodic boundary, c.f. Figure 2.2).

at the new inlet to the machine, which is stronger than in the base cases.

The fan blades cause an even stronger pressure build-up within the machine, which drives the flow more inwards in the presence of a stator baffle. This helps minimizing the upward flow near the stator inner wall. The cases with a stator baffle show an obvious separation bubble at the tip of the stator baffle. The separation happens because the fluid flows normal to the baffle at the inlet. However, the separation zone gets smaller in size when the fan blades are introduced. This is because the flow rates are higher with use of fan blades, which is again caused by larger pressure gradients in the domain.

The cases with stator baffles show less strong upwards velocities above the rotor poles, again caused by the pressure build-up in the machine, which strengthens the inward flow inside the machine. The fan blades help to almost remove the upward-velocity regions through generating an even higher pressure in the region which pushes even more flow through the stator channels. The correspondingly higher volume flows clarifies this. This does not apply to case *C7F*.

2.5 Flow in the Channels

Tables 2.6 and 2.7 show the recirculation zones in the upper and the lower stator channels respectively. The shaded areas show the regions with negative radial velocity. The visualization is made in a plane in the middle of the channel heights.

Cases without fan blades show large recirculation regions to the right side of the stator windings, when seen from inside. The cases including fan blades show considerably smaller recirculation areas compared to other cases, and that is mainly visible just behind, or to a small extent, to the right side of the windings. This does not apply to case *C7F*, in which the flow in both the upper and lower channel rows is associated with strong recirculations. This means that in cases without a fan blade, the air is pushed into the channels from one side of the stator windings. This is caused by the relatively high pressure difference between inside and outside of the channels. In the air gap between rotor and stator, separation occurs just to the right side of the stator windings (when seen from inside) and makes a low pressure region there. The low pressure region draws the air from the high pressure region inside the channels, which is undesirable. In cases with fan blades (except *C7F*), however, the air enters the channels mostly from both sides of the stator windings. This is caused by the larger pressure build-up inside the machine and leads to a higher flow rate. For cases

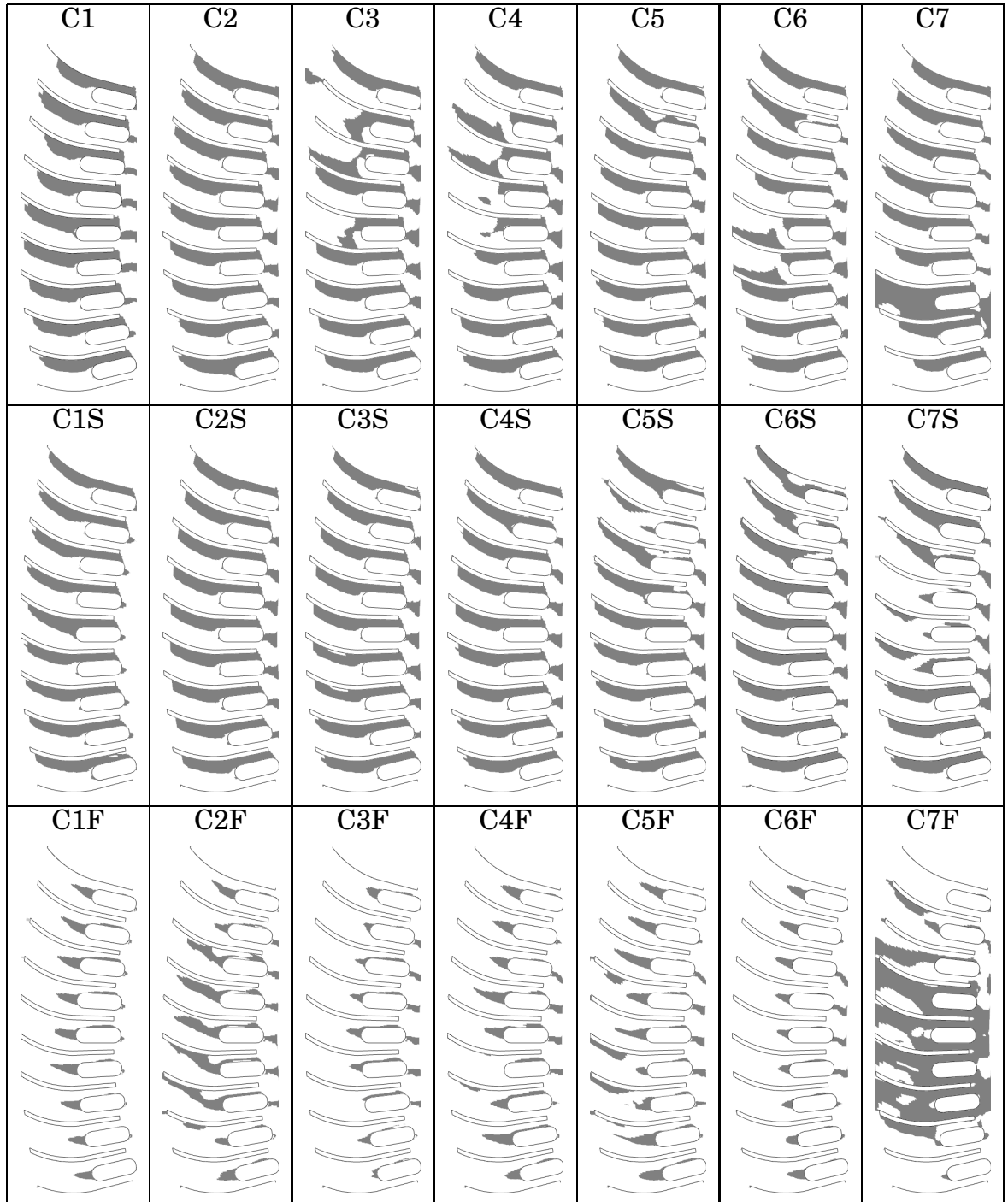


Table 2.6: Flow in the middle of the upper channel row: The shaded areas show regions with negative radial velocity.

CHAPTER 2. CASES AND RESULTS

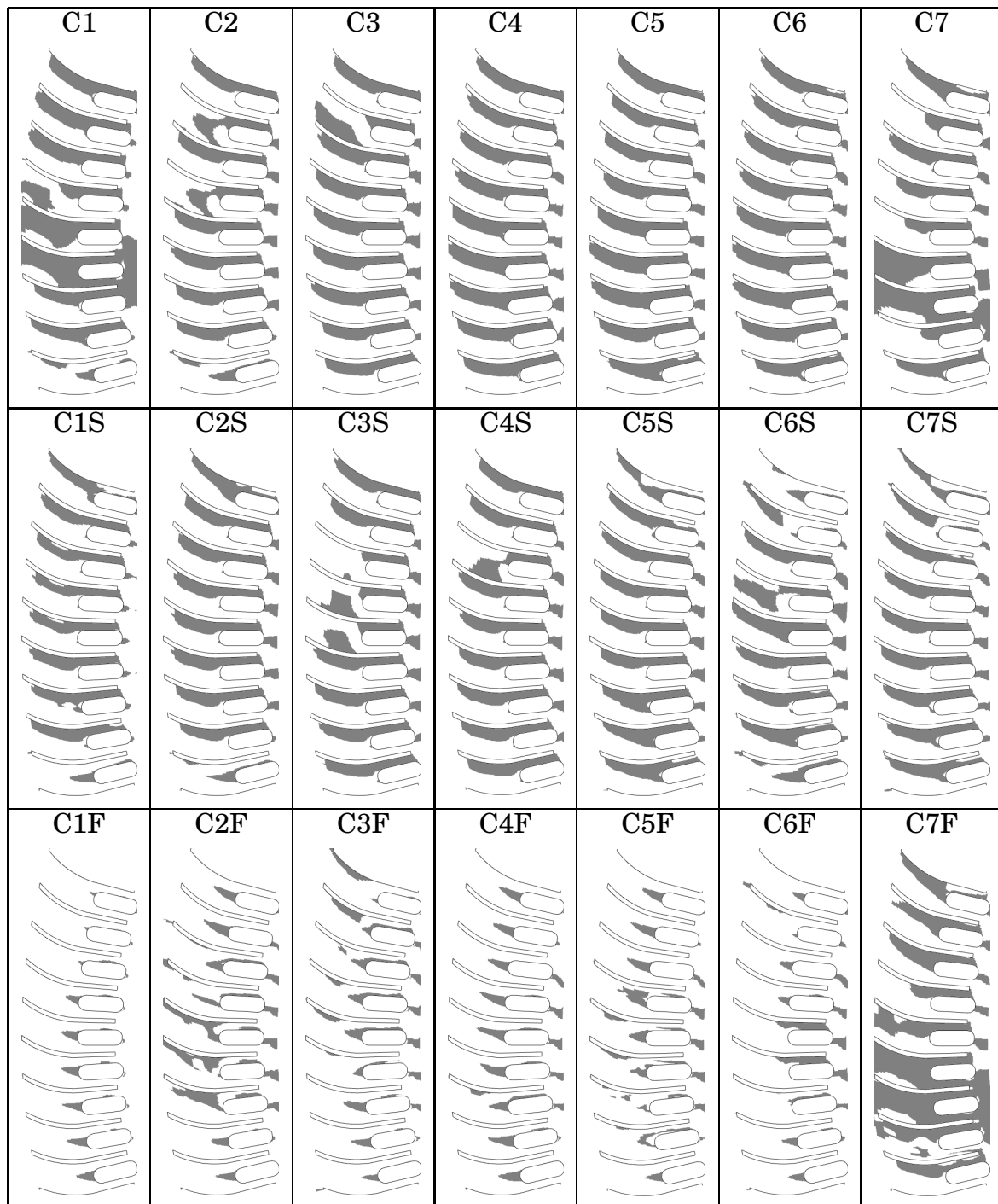


Table 2.7: Flow in the middle of the lower channel row: The shaded areas show regions with negative radial velocity.

C1, C7 and *C7F* the flow in some channels has purely negative radial velocities. This means that the fluid flows from the channel into the machine, which is undesirable.

2.6 Velocity Components Just Above the Rotor Poles

In table 2.8-2.10 the velocity components are analyzed in a plane just above the rotor poles. A distance of $0.2mm$ is chosen between the contours and the pole upper surface.

Table 2.8 shows the axial velocity component just above the rotor poles. A positive sign means that the axial velocity component is directed upwards. In certain cases a region of upward axial velocities are visible, which is not desirable as one would ideally expect inward axial velocities at this location. As Table 2.8 suggests, except for the cases *C7S* and *C7F*, the use of stator baffles, as well as the combination of the stator baffles and fan blades on top of the rotor poles, helps decreasing the upward axial velocities and increasing the downward axial velocities in the region between the rotor and the stator. This means that the air flow inside the machine generally increases with the use of stator baffles and fan blades. This is, however, not the case for the *C7S* and *C7F*.

Table 2.9 shows the tangential velocity components just above the rotor poles. According to the right-hand rule with rotational axis pointing outward from the pictures, a negative sign means that the rotation takes place clockwise, which in this case means upwards in the pictures. Adding a baffle to the stator reduces the average tangential velocity. However, adding fan blades helps recovering the high value of the tangential velocity through supplying kinetic energy to the air. For each pole design the highest tangential velocity is achieved with a fan blade. Rounded pole edges leads to larger tangential components just above the rotor. Case *C7F* again shows an unusual distribution of tangential velocities. As the velocity components are shown just above the rotor pole, one would expect the velocities to more or less follow those of the pole at each diameter. This is, however, obviously not the case for *C7F* which has strong positive tangential velocities in some regions. This may indicate that there are strong recirculations.

Table 2.10 shows the radial velocity component just above the rotor poles. A positive sign means that the velocity is directed radially outwards. In the air gap between the rotor and stator in the cases without a fan blade, there is a region with negative radial velocities, which

CHAPTER 2. CASES AND RESULTS

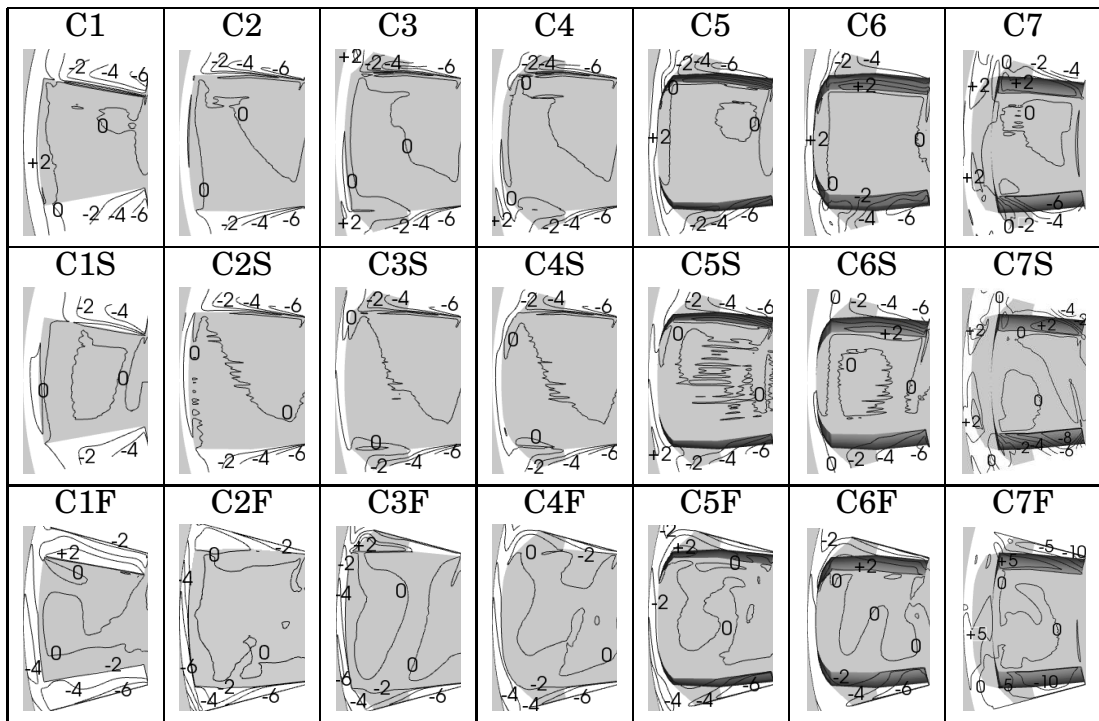


Table 2.8: Axial velocity just above the rotor poles (m/s)

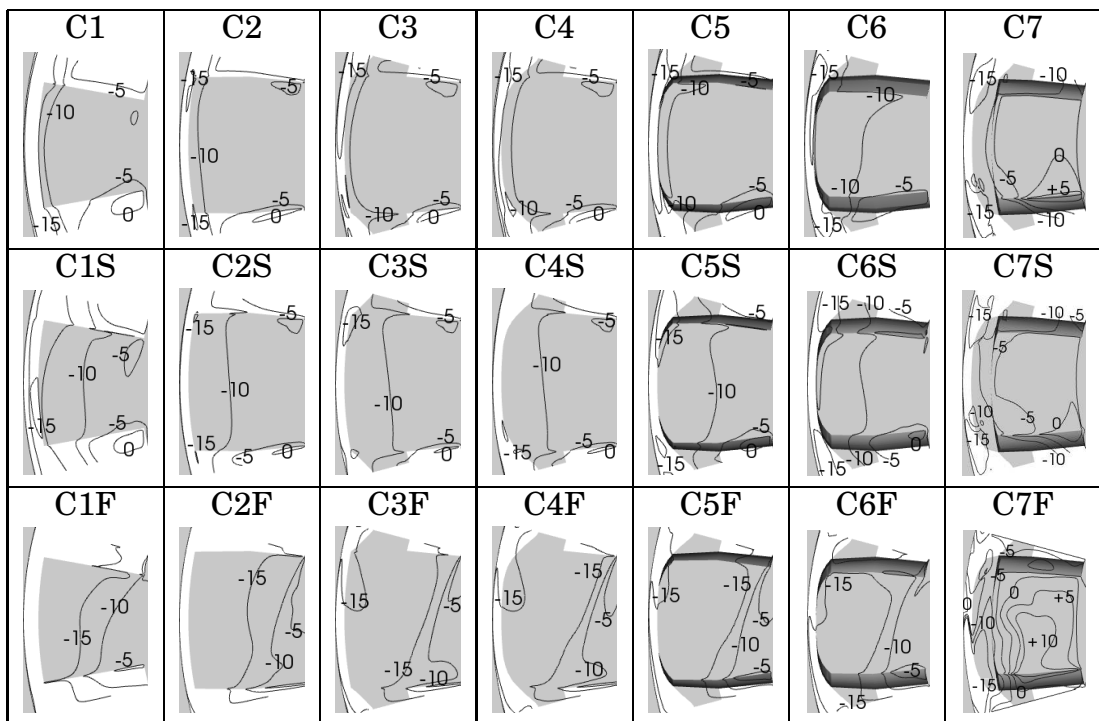


Table 2.9: Tangential velocity just above the rotor poles (m/s)

shows a recirculation between the poles. In the cases with a fan blade, however, the recirculation area is located in between two adjacent fan blades.

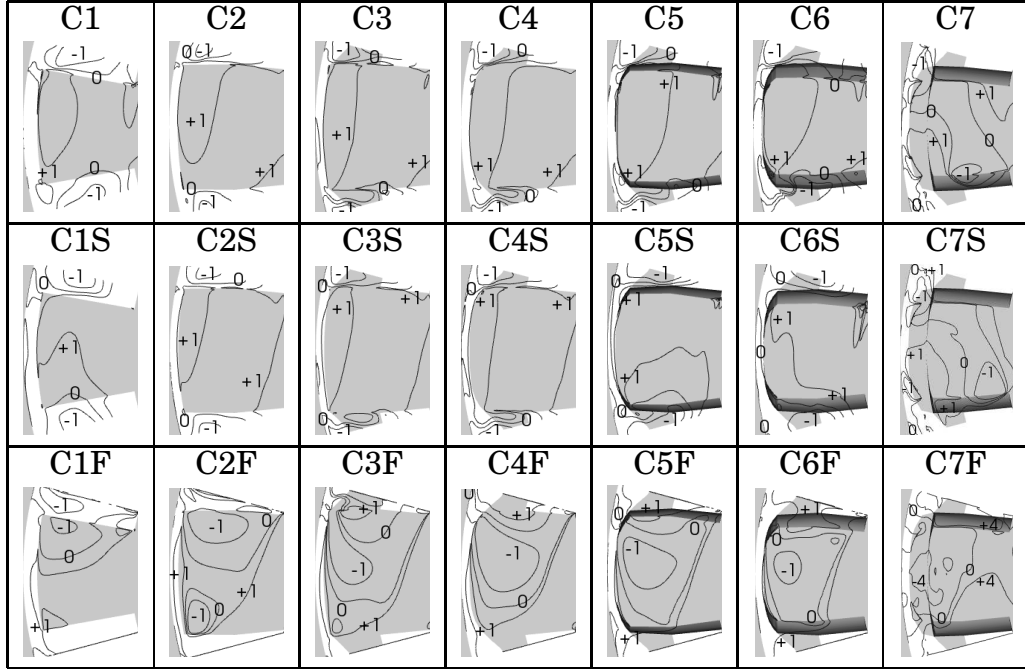


Table 2.10: Radial velocity just above the rotor poles (m/s)

2.7 Relative Tangential Velocity in the Pole Gap

The tangential velocity *relative* to the rotor pole is shown in Table 2.11. The relative component is taken on a plane normal to the axis of rotation and at a height in the middle of the stator channels. The relative velocity component is computed through the relation

$$u_{tangential,relative} = u_{tangential} - \omega r$$

where ωr is the tangential velocity of the pole at radius r . Table 2.11 suggests that the tangential velocity in the middle of the stator channels is more or less following the pole tangential velocity, with small differences in certain regions. Near the stator wall the tangential velocity decreases as the fluid gets close to the walls.

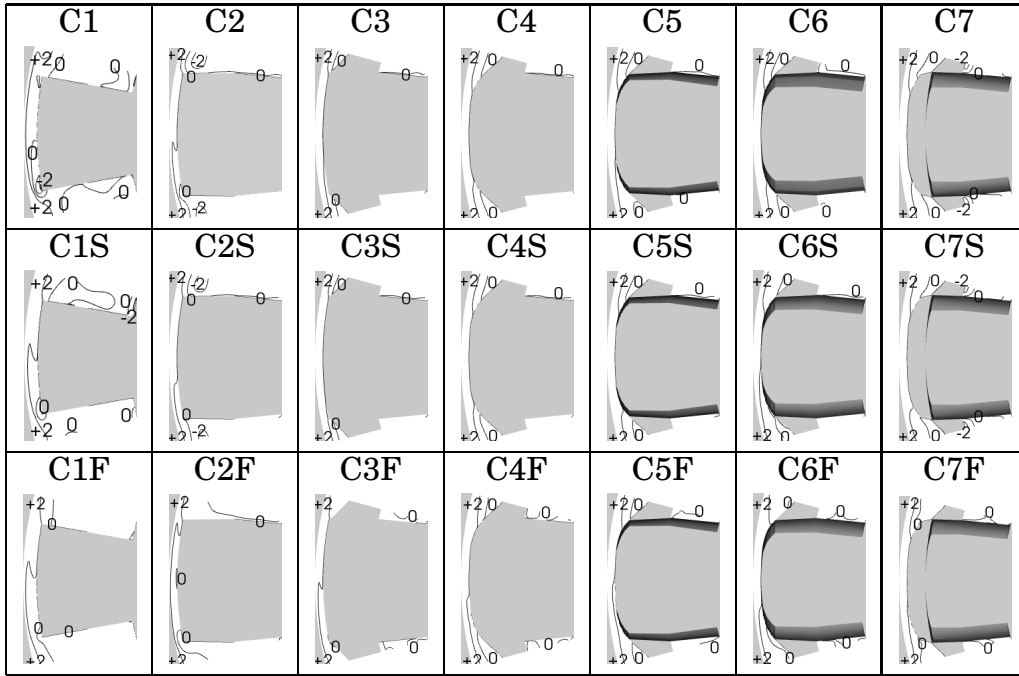


Table 2.11: Relative tangential velocity, between the stator channels (m/s)

2.8 Pressure Distributions on the Rotor Poles

Tables 2.12, 2.13, 2.14 and 2.15 show the contours of the quantity $(\frac{p-p_{ref}}{\rho})$ on the pole top, pole pressure side, pole suction side and pole front. The quantity p refers to the static pressure at each point, while p_{ref} is the static pressure at a reference cell. The reference cell is located just at the top-outer edge of the domain. The reference point is, thus, located outside the stator and is identical for all cases. The quantity ρ is the air density.

According to the tables 2.12-2.14, near the rotor body there is a region with relatively lower $(\frac{p-p_{ref}}{\rho})$ values. This means that the static pressure is low in that region, which causes the air to be sucked stronger into the machine and gives a larger inward velocity.

The quantity $(\frac{p-p_{ref}}{\rho})$ gives a reasonable picture of how the volume flow should be distributed in the channels. In cases with smaller variations in p_{stat} , and thus smaller variations on $(\frac{p-p_{ref}}{\rho})$, less differences between the volume flow distributions in the channels is noticed. A good example in this case is the base cases without the stator baffles. On the other hand, in cases with larger variations in p_{stat} the volume flow is less evenly distributed and the differences between the flow in different channels can be seen. This particularly applies for the cases

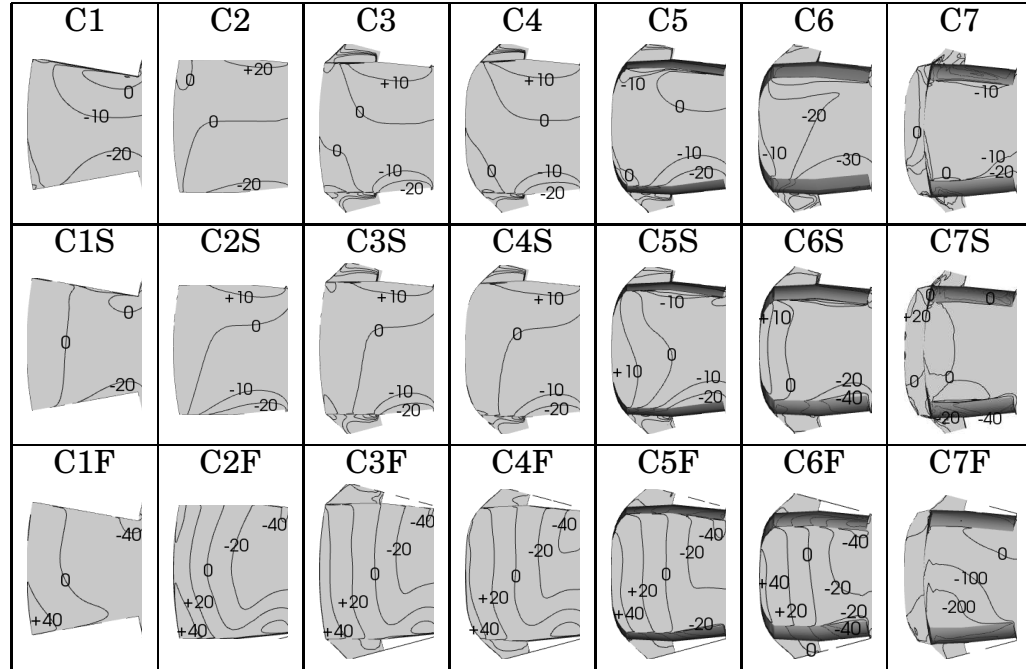


Table 2.12: Contours of relative static pressure divided by density, ($\frac{p-p_{ref}}{\rho}$) [m²/s²], on the pole top

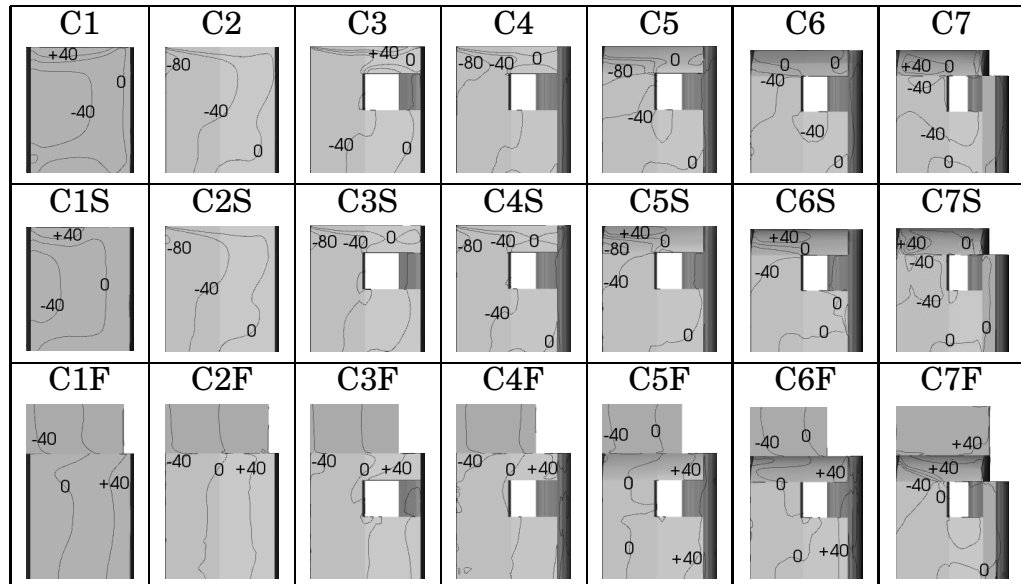


Table 2.13: Contours of relative static pressure divided by density, ($\frac{p-p_{ref}}{\rho}$) [m²/s²], on the pole pressure side

CHAPTER 2. CASES AND RESULTS

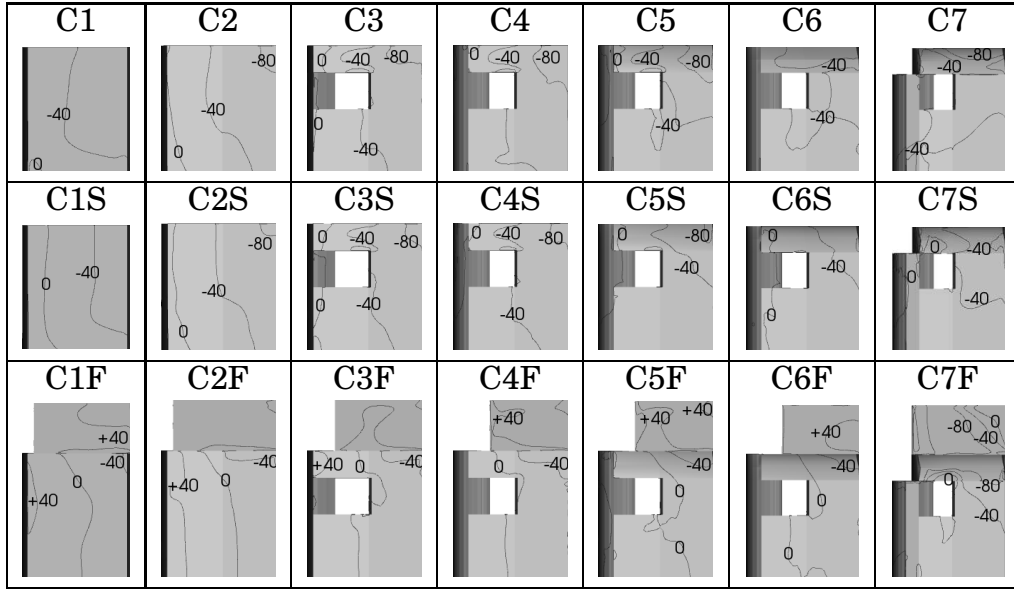


Table 2.14: Contours of relative static pressure divided by density, ($\frac{p-p_{ref}}{\rho}$) [m²/s²], on the pole suction side

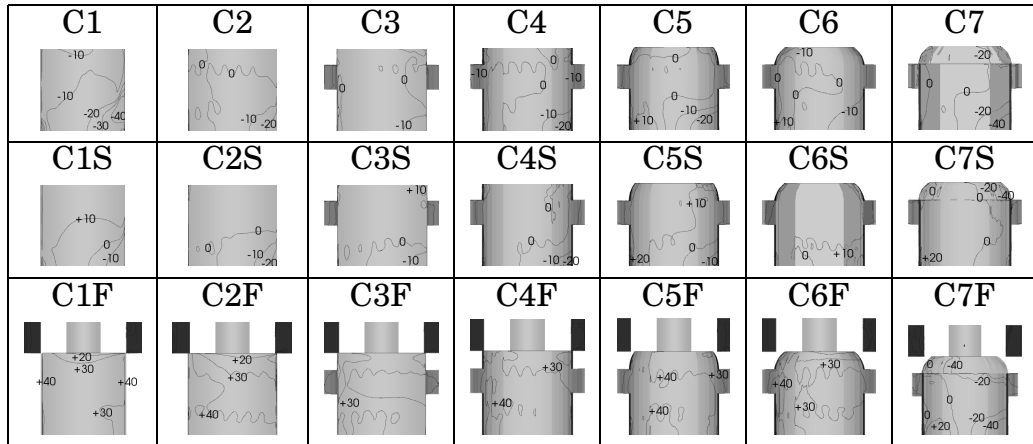


Table 2.15: Contours of relative static pressure divided by density, ($\frac{p-p_{ref}}{\rho}$) [m²/s²], on the pole front

with fan blades.

Chapter 3

Concluding Remarks and Future Work

DIFFERENT rotor pole and stator geometries of a generator were tested with the purpose of investigating the air flow through the machine. The numerical results obtained using OpenFOAM were compared to each other. According to the computational results, addition of baffles at the inlet of the stator helps increasing the volume flow within the machine and removes the outward velocities at the inlet. Furthermore, adding fan blades on top of the rotor poles generally increases the volume flow inside the machine. This, however, is not the case for the last geometric modification.

The air flow separates in the stator channels. However, addition of the baffle to the stator inlet together with fan blades on top of the rotor pole generally helps to minimize the separation zone. This is, again, not the case for the last geometric modification.

The axial power needed by the rotor is shown to decrease by using the stator blades. However, adding fan blades to the rotor poles leads to an increased rotor axial power. The last geometric modification, however, is an exempt to this.

Experimental data are needed to validate the computational results with. In the continuation of the present work, experiments will be performed on the real generator to measure the velocity and pressure distributions at the inlet and the outlet of the machine. The experimental results will then be compared to the computations to examine the quality of the computations.

The current computations were performed using the frozen-rotor concept (See Appendix A). This means that the cases are run quasi-steady. The solution quality would be higher with unsteady computations. Thus, the future focus of the work will be on running transient cases with rotating mesh.

Different incompressible RAS turbulence models in OpenFOAM-1.5.x were studied and the implementations were compared to the original models. The implementation of some models or model coefficients differ from the original models to a certain degree. This is described in Appendix A. In Appendix B, two validation test cases are described: a backward facing step test case and a laminar Couette flow test case. In the former test case, almost all turbulence models described in Appendix A were tested on a backward facing step to compare the numerical results of the turbulence models implemented in OpenFOAM-1.5.x with experimental data on the same test case, and to select the most appropriate turbulence model for the computation of air flow in the generator. The results suggest that the RNGkEpsilon and Launder-SharmaKE turbulence models show the best level of consistency with the experimental data. Finally, a laminar Couette flow test case was run between two concentric cylinders and the numerical velocity and pressure distributions between the cylinders were compared to the analytical results. The results proved to be very much alike. More discussions on validation test cases are found in Appendix B.

Appendices

Appendix A

Modeling

THE air flow in an electric generator is rather complex and the velocities involved are in the turbulent flow regime. Therefore, a suitable set of equations, discretization schemes and turbulence models should be chosen to predict the flow. In the present work, the steady-state Reynolds-Averaged Navier-Stokes equations are solved using the finite volume method and the Frozen Rotor approach. The OpenFOAM-1.5.x CFD toolbox is used for the simulations. A block-structured mesh is generated by the built-in blockMesh mesh generator, and m4 parametrization. The convective terms in the momentum and turbulence equations are discretized using the first-order upwind scheme. In this work, the choice of turbulence model has been limited to steady RANS models. In order to select the most suitable turbulence model to simulate the generator case, a number of RANS turbulence models in OpenFOAM have been validated in the backward facing step test case. Further, to verify that OpenFOAM correctly predicts the build-up of the pressure due to the rotation, the laminar flow in a concentric cylinder test case has been studied. In the following sections the numerical methods are first described, followed by the validations for the two test cases.

A.1 Turbulence Models

Generally, RANS turbulence models are divided into two main groups, the ones integrating up to the wall (low-Re) and those with wall functions (high-Re). The former group solves the equations up to the wall surface and thus needs a very fine mesh near the walls to be able to capture the large gradients in that region. The mesh sizes in the near-wall region should satisfy the general requirement of $y^+ \approx 1$ everywhere. This requires very fine cells, a large memory usage and long simulation times. It is thus of interest to model the near-wall gradi-

ents, rather than solving them. This is done by introducing the so-called wall functions. In this method, the center of the first cell in the vicinity of the wall should be located in the overlap region of the wall boundary layer ($30 < Y^+ < 100$) and thus the wall shear stresses are computed through the logarithmic law. In this way, the fine mesh in the boundary layer region will be replaced by a coarse one and thus the gradients near the walls are modelled in a single cell. The computational memory and time will be saved tremendously with this method.

The low-Re turbulence models include extra source terms and damping functions to correctly model the near-wall behaviour. Typically, two functions f_1 and f_2 are added to the ε equation, function f_μ is added to the modeling of ν_t and source terms D and E are added to the k and ε equations respectively.

In the following sections all of the incompressible RANS turbulence models in OpenFOAM-1.5.x are described briefly. Each description states if the model is high-Re or low-Re shows the mathematical notation, and the way it is implemented in OpenFOAM-1.5.x. First a brief description of OpenFOAM notations is discussed.

A.1.1 Mathematical Notation in OpenFOAM

In the descriptions of the turbulence models of OpenFOAM-1.5.x in the following sections, it is also described how the equations are implemented in the code. Table A.1 is provided to relate the mathematical and OpenFOAM (code) notations for some of the most important operators in this context. Further description of OpenFOAM operators can be found in the OpenFOAM programmers guide.

The implementation of the material derivative is here described using the convection of the turbulent kinetic energy, k , as an example. The material derivative is expressed as

$$\frac{Dk}{Dt} = \frac{\partial k}{\partial t} + U \cdot \nabla k$$

The last term can be re-written as

$$U \cdot \nabla k = \nabla \cdot (Uk) - (\nabla \cdot U)k$$

The last term in this equation is zero in an incompressible formulation ($\nabla \cdot U = 0$). However, during convergence it is non-zero, and the term is sometimes kept to improve the convergence rate [1]. Looking at the actual implementation in OpenFOAM, this expression is written as

```
fvm::div(phi_,k_)-fvm::Sp(fvc::div(phi_),k)
```

APPENDIX A. MODELING

The nomenclature `fvm::` means that both terms will be introduced in the coefficient matrix. The first term will use the control volume face flux (`phi_`) to calculate the divergence of U_k , using Gauss theorem (looping over the control volume faces). The second term will explicitly (`fvc::`) calculate the divergence of U , again using the Gauss theorem, and introducing the term in the coefficient matrix (`fvm ::`) by a multiplicatuib by k through the source term implementation (`Sp`).

Description	Mathematical expression	OpenFOAM expression
Deviatoric component	$devT$ ¹	<code>dev(T)</code>
Divergence	$\nabla \cdot \chi$	<code>div(chi)</code>
Double inner product	$a : b$ ²	<code>a && b</code>
Gradient	$\nabla \phi$	<code>grad(phi)</code>
Identity tensor	δ_{ij}	<code>I</code>
Inner product	$a \cdot b$	<code>a & b</code>
Laplacian	$\nabla \cdot \Gamma \nabla \phi$	<code>laplacian(gamma,phi)</code>
Magnitude squared	$ a ^2$	<code>magSqr(a)</code>
Rotation tensor	Ω_{ij}	<code>skew(fvc::grad(U))</code>
Skew tensor	$skewT$	<code>skew(T)</code>
Strain tensor	S_{ij}	<code>symm(fvc::grad(U))</code>
Symmetric tensor	$symmT$	<code>symm(T)</code>
Trace	trT	<code>tr(T)</code>
Transpose	T^T	<code>T.T()</code>
	$2 * SymmT$	<code>twoSymm(T)</code>
	$ \nabla \nabla \phi ^2$	<code>magSqrGradGrad(phi)</code>

Table A.1: OpenFOAM mathematical notations

¹Deviatoric Component of a tensor T :

$$dev(T) = T - \frac{1}{3}tr(T)I$$

²The "Double Inner Product" of the two second rank tensors a and b . It is a scalar which is computed through $a_{ij}b_{ij}$, as:

$$s = \begin{cases} a_{11}b_{11} + a_{12}b_{12} + a_{13}b_{13} \\ + a_{21}b_{21} + a_{22}b_{22} + a_{23}b_{23} \\ + a_{31}b_{31} + a_{32}b_{32} + a_{33}b_{33} \end{cases}$$

A.1.2 kEpsilon

The kEpsilon model is the standard high-Re $k - \varepsilon$ model with wall functions [2]. It is implemented in OpenFOAM as

$$\frac{\partial k}{\partial t} + \nabla \cdot (Uk) - (\nabla \cdot U)k - \nabla \cdot D_{k,eff} \nabla k = G - \varepsilon$$

$$\frac{\partial \varepsilon}{\partial t} + \nabla \cdot (U\varepsilon) - (\nabla \cdot U)\varepsilon - \nabla \cdot D_{\varepsilon,eff} \nabla \varepsilon = C_{\varepsilon 1} \frac{\varepsilon}{k} G - C_{\varepsilon 2} \frac{\varepsilon^2}{k}$$

G	$D_{k,eff}$	$D_{\varepsilon,eff}$	α_ε	ν_t	$C_{\varepsilon 1}$	$C_{\varepsilon 2}$	C_μ
$\nu_t 2 S_{ij} ^2$	$\nu + \nu_t$	$\nu + \alpha_\varepsilon \nu_t$	0.76923	$C_\mu \frac{k^2}{\varepsilon}$	1.44	1.92	0.09

The appropriate turbulence boundary conditions at the walls are $\partial k / \partial \hat{n}|_{wall} = 0$ and $\partial \varepsilon / \partial \hat{n}|_{wall} = 0$, where \hat{n} is the unit vector normal to the wall.

The k and ε equations in the original model [2] are written as

$$\frac{Dk}{Dt} = \frac{\partial}{\partial x_j} \left[(\nu + \frac{\nu_t}{\sigma_k}) \frac{\partial k}{\partial x_j} \right] + P_k - \varepsilon$$

$$\frac{D\varepsilon}{Dt} = \frac{\partial}{\partial x_j} \left[(\nu + \frac{\nu_t}{\sigma_\varepsilon}) \frac{\partial \varepsilon}{\partial x_j} \right] + C_{\varepsilon 1} \frac{\varepsilon}{k} P_k - C_{\varepsilon 2} \frac{\varepsilon^2}{k}$$

ν_t	P_k	S	S_{ij}	$C_{\varepsilon 1}$	$C_{\varepsilon 2}$	C_μ	σ_k	σ_ε
$C_\mu \frac{k^2}{\varepsilon}$	$\nu_t S^2$	$\sqrt{2S_{ij}S_{ij}}$	$\frac{1}{2}[U_{i,j} + U_{j,i}]$	1.44	1.92	0.09	1	1.3

A.1.3 RNGkEpsilon

The RNGkEpsilon model is variant of the $k - \varepsilon$ model, which is based on the "Re-Normalization Groups" method [3]. It is also a high-Re model using wall functions. Using the RNG method, the Navier-Stokes equations are renormalized to be able to deal with smaller scale effects. In the standard $k - \varepsilon$ model the eddy viscosity is based on a single turbulent length scale, while in reality all scales of motion affect the turbulent diffusion. The model is implemented in OpenFOAM as

$$\frac{\partial k}{\partial t} + \nabla \cdot (Uk) - \nabla \cdot D_{k,eff} \nabla k = G - \varepsilon$$

$$\frac{\partial \varepsilon}{\partial t} + \nabla \cdot (U\varepsilon) - \nabla \cdot D_{\varepsilon,eff} \nabla \varepsilon = (C_{\varepsilon 1} - R) \frac{\varepsilon}{k} G - C_{\varepsilon 2} \frac{\varepsilon^2}{k}$$

APPENDIX A. MODELING

R	η	S_2	$D_{k,eff}$	$D_{\varepsilon,eff}$	G
$\eta \frac{1 - \left(\frac{\eta}{\eta_0}\right)}{1 + \beta \eta^3}$	$\sqrt{S_2} \frac{k}{\varepsilon}$	$2 S_{ij} ^2$	$\nu + \alpha_k \nu_t$	$\nu + \alpha_\varepsilon \nu_t$	$\nu_t S_2$
α_k	α_ε	C_μ	$C_{\varepsilon 1}$	$C_{\varepsilon 2}$	β
1.39	1.39	0.0845	1.42	1.68	0.012

ν_t has the same formulation as in the kEpsilon model. The appropriate turbulence boundary conditions at the walls are $\partial k / \partial \hat{n}|_{wall} = 0$ and $\partial \varepsilon / \partial \hat{n}|_{wall} = 0$, where \hat{n} is the unit vector normal to the wall.

In the original model [3], the k -equation is the same as in the standard $k-\varepsilon$ model, while the production term in the ε equation is modified according to

$$\frac{D\varepsilon}{Dt} = \frac{\partial}{\partial x_j} \left[(\nu + \frac{\nu_t}{\sigma_\varepsilon}) \frac{\partial \varepsilon}{\partial x_j} \right] + C_{\varepsilon 1}^* \frac{\varepsilon}{k} P_k - C_{\varepsilon 2} \frac{\varepsilon^2}{k}$$

$C_{\varepsilon 1}^*$	η	η_0	β	$C_{\varepsilon 1}$	$C_{\varepsilon 2}$	C_μ	σ_k	σ_ε
$C_{\varepsilon 1} - \left[\frac{\eta(1 - \frac{\eta}{\eta_0})}{1 + \beta \eta^3} \right]$	Sk/ε	4.38	0.015	1.42	1.68	0.085	0.7179	0.7179

P_k , ν_t , S and S_{ij} follow the same formulations as in the standard $k - \varepsilon$ model.

A.1.4 realizableKE

The realizableKE model is the high-Re realizable $k - \varepsilon$ model with wall functions [4]. A turbulence model is realizable if the normal stresses remain positive, that is $\overline{u_i'^2} \geq 0$ for all i . The model is implemented in OpenFOAM as

$$\begin{aligned} \frac{\partial k}{\partial t} + \nabla \cdot (U k) - (\nabla \cdot U) k - \nabla \cdot D_{k,eff} \nabla k &= G - \varepsilon \\ \frac{\partial \varepsilon}{\partial t} + \nabla \cdot (U \varepsilon) - (\nabla \cdot U) \varepsilon - \nabla \cdot D_{\varepsilon,eff} \nabla \varepsilon &= C_{\varepsilon 1} |S| \varepsilon - C_{\varepsilon 2} \frac{\varepsilon^2}{k + \sqrt{\nu \varepsilon}} \end{aligned}$$

$C_{\varepsilon 1}$	η	$ S $	S_2	W
$\max(0.43, \left(\frac{\eta}{\eta+5}\right))$	$ S k/\varepsilon$	$\sqrt{S_2}$	$2 dev(S_{ij}) ^2$	$2\sqrt{2} \left(\frac{(S \cdot S) : S}{ S S_2}\right)$
$C\mu$	A_s		ϕ^*	G
$\left(\frac{1}{A_0 + A_s \left(\frac{kU^*}{\varepsilon}\right)}\right)$	$\sqrt{6} \cos \phi^*$	$\frac{1}{3} \cos^{-1} (\min(\max(\sqrt{6}W, -1), 1))$		$\nu_t S_2$
U^*	A_0	$C_{\varepsilon 2}$	α_k	α_ε
$\sqrt{\frac{S_2}{2}} + \Omega_{ij} ^2$	4.0	1.9	1	0.833

ν_t , $D_{k,eff}$ and $D_{\varepsilon,eff}$ have the same formulations as in the RNGkEpsilon model. The appropriate turbulence boundary conditions at the walls are $\partial k / \partial \hat{n}|_{wall} = 0$ and $\partial \varepsilon / \partial \hat{n}|_{wall} = 0$, where \hat{n} is the unit vector normal to the wall.

In the original model [4], the k equation is the same as in the standard $k - \varepsilon$ model, while the ε equation is written as

$$\frac{D\varepsilon}{Dt} = \frac{\partial}{\partial x_j} \left[(\nu + \frac{\nu_t}{\sigma_\varepsilon}) \frac{\partial \varepsilon}{\partial x_j} \right] + C_{\varepsilon 1} S \varepsilon - C_{\varepsilon 2} \frac{\varepsilon^2}{k + \sqrt{\nu \varepsilon}}$$

$C_{\varepsilon 1}$	$C\mu$	A_s
$\max(0.43, \left(\frac{\eta}{\eta+5}\right))$	$\left(\frac{1}{A_0 + A_s \left(\frac{kU^*}{\varepsilon}\right)}\right)$	$\sqrt{6} \cos \phi$
ϕ	S	\tilde{S}
$\frac{1}{3} \cos^{-1}(\sqrt{6}W)$	$\sqrt{2S_{ij}S_{ij}}$	$\sqrt{S_{ij}S_{ij}} \left(\frac{S_{ij}S_{jk}S_{ki}}{\tilde{S}^3}\right)$
U^*	$\widetilde{\Omega}_{ij}$	Ω_{ij}
$\sqrt{S_{ij}S_{ij} + \widetilde{\Omega}_{ij}\widetilde{\Omega}_{ij}}$	$\Omega_{ij} - 2\varepsilon_{ijk}\omega_k$	$\overline{\Omega}_{ij} - \varepsilon_{ijk}\omega_k$
A_0	$C_{\varepsilon 2}$	σ_k
4.0	1.9	1
		σ_ε
		1.2

Here $\overline{\Omega}_{ij}$ is the mean rate of rotation tensor viewed in a rotating reference frame with an angular velocity ω_k . Notice that the rotation of the reference system is NOT included in OpenFOAM. The quantities P_k , ν_t , S_{ij} and η follow the same formulations as in the RNG $k - \varepsilon$ model.

A.1.5 kOmegaSST

The kOmegaSST model is the high-Re $k - \omega$ SST model with wall functions [5]. The model uses the $k - \omega$ model in the regions of the boundary

APPENDIX A. MODELING

layer and switches to the $k - \varepsilon$ model elsewhere. The OpenFOAM implementation of the model reads

$$\frac{\partial k}{\partial t} + \nabla \cdot (Uk) - (\nabla \cdot U)k - \nabla \cdot D_{k,eff}(F_1)\nabla k = \min(G, C_{\varepsilon 1}\beta^*k\omega) - \beta^*\omega k$$

$$\frac{\partial \omega}{\partial t} + \nabla \cdot (U\omega) - (\nabla \cdot U)\omega - \nabla \cdot D_{\omega,eff}(F_1)\nabla \omega = \gamma(F_1)2S^2 - \beta(F_1)\omega^2 + (1 - F_1)CD_{k\omega}$$

$F_1(CD_{k\omega})$					
$\tanh \left[\min(\min(\max(\frac{\sqrt{k}}{\beta^*\omega y}, \frac{500\nu}{y^2\omega}), (\frac{4\rho\sigma_{\omega 2}k}{\max(CD_{k\omega}, 1^{-10})y^2}), 10) \right]^4 \right]$					
F_2					
$\tanh \left[\min(\max(\frac{2\sqrt{k}}{\beta^*\omega y}, \frac{500\nu}{y^2\omega}), 100) \right]^2 \right]$					
$CD_{k\omega}$	G	S_2	ν_t	β^*	
$2\alpha_{\omega 2}\frac{\nabla k + \nabla \omega}{\omega}$	$\nu_t 2S_2$	$ S_{ij} ^2$	$\left(\frac{a_1 k}{\max(a_1 \omega, \sqrt{S_2} F_2)} \right)$	0.09	
α_{k1}	α_{k2}	$\alpha_{\omega 1}$	$\alpha_{\omega 2}$	γ_1	γ_2
0.85034	1.0	0.5	0.85616	0.5532	0.4403
β_1	β_2	$C_{\varepsilon 1}$	$C_{\varepsilon 2}$	κ	a_1
0.0750	0.0828	10	1.92	0.41	10
$D_{k,eff}(F_1)$			$D_{\omega,eff}(F_1)$		
$\nu + \alpha_k(F_1)\nu_t$			$\nu + \alpha_\omega(F_1)\nu_t$		

The appropriate turbulence boundary conditions at the walls are $\partial k / \partial \hat{n}|_{wall} = 0$ and $\partial \omega / \partial \hat{n}|_{wall} = 0$, where \hat{n} is the unit vector normal to the wall. The model coefficients are found by means of the blending function F_1 , which is equal to 1 in the near-wall regions and 0 in the outer part of the boundary layer. In this way, a model coefficient ϕ is a function of the variable F_1 and is found through the relation

$$\phi(F_1) = \phi_1 F_1 + \phi_2 (1 - F_1)$$

Here ϕ_1 and ϕ_2 are the coefficients for the $k - \omega$ and $k - \varepsilon$ models respectively.

The original model [5] reads

$$\frac{Dk}{Dt} = \min(P_k, C_{\varepsilon 1}\varepsilon) - \beta^*k\omega + \frac{\partial}{\partial x_j} \left[(\nu + \frac{\nu_t}{\sigma_k}) \frac{\partial k}{\partial x_j} \right]$$

$$\frac{D\omega}{Dt} = \frac{\gamma}{\nu_t} P_k - \beta\omega^2 + \frac{\partial}{\partial x_j} \left[(\nu + \frac{\nu_t}{\sigma_\omega}) \frac{\partial \omega}{\partial x_j} \right] + 2(1 - F_1)\sigma_{\omega 2} \frac{1}{\omega} \frac{\partial k}{\partial x_j} \frac{\partial \omega}{\partial x_j}$$

F_1			F_2		
$\tanh \left[\left[\min(\max(\frac{\sqrt{k}}{\beta^* \omega y}, \frac{500\nu}{y^2 \omega}), (\frac{4\rho\sigma_{\omega 2} k}{CD_{k\omega} y^2}) \right]^4 \right]$			$\tanh \left[\left[\max(\frac{2\sqrt{k}}{\beta^* \omega y}, \frac{500\nu}{y^2 \omega}) \right]^2 \right]$		
$CD_{k\omega}$		ν_t		P_k	
$\max(2\rho\sigma_{\omega 2} \frac{1}{\omega} \frac{\partial k}{\partial x_j} \frac{\partial \omega}{\partial x_j}, 10^{-10})$		$\left(\frac{a_1 k}{\max(a_1 \omega, SF_2)} \right)$		$\tau_{ij} \frac{\partial U_i}{\partial x_j}$	
σ_{k1}	σ_{k2}	$\sigma_{\omega 1}$	$\sigma_{\omega 2}$	γ_1	γ_2
1.176	1.000	2.000	1.168	0.5532	0.4403
β_1	β_2	β^*	κ	a_1	$C_{\varepsilon 1}$
0.0750	0.0828	0.09	0.41	10	10

Here $\varepsilon = \beta^* k \omega$ and the quantities P_k , S , and S_{ij} follow the same formulations as standard $k - \varepsilon$ model.

A.1.6 NonlinearKEShih

The NonlinearKEShih model is the high-Re non-linear Shih $k - \varepsilon$ model with wall functions [6], also known as the Realizable Reynolds Stress Algebraic Equation (RRSAE) model. The OpenFOAM implementation reads

$$\begin{aligned} \frac{\partial k}{\partial t} + \nabla \cdot (U k) - \nabla \cdot D_{k,eff} \nabla k &= G - \varepsilon \\ \frac{\partial \varepsilon}{\partial t} + \nabla \cdot (U \varepsilon) - \nabla \cdot D_{\varepsilon,eff} \nabla \varepsilon &= C_{\varepsilon 1} \frac{\varepsilon}{k} G - C_{\varepsilon 2} \frac{\varepsilon^2}{k} \end{aligned}$$

T_{ij}					
<i>symm</i>	$\frac{k^3}{\varepsilon^2}$	$\frac{C_{\tau 1}}{f_\eta} ((U_{i,k} \cdot U_{k,j} + U_{k,i} \cdot U_{j,k})) + \frac{C_{\tau 2}}{f_\eta} ((U_{i,k} \cdot U_{j,k})) + \frac{C_{\tau 3}}{f_\eta} (U_{k,i} \cdot U_{k,j})$			
G		f_η	S_2	ν_t	C_μ
$C_\mu \frac{k^2}{\varepsilon} S_2 - (T_{ij} : U_{i,j})$		$A_2 + \eta^3$	$S_{ij} : U_{i,j}$	$C_\mu \left(\frac{k^2}{\varepsilon} \right)$	$\left(\frac{2/3}{A_1 + \eta + \alpha_\xi \xi} \right)$
η		ξ	α_ε	α_k	α_ξ
$\frac{k}{\varepsilon} \sqrt{2 U_{i,j} + U_{j,i} ^2}$		$\frac{k}{\varepsilon} \sqrt{2 U_{i,j} - U_{j,i} ^2}$	0.76923	1	0.9
$C_{\tau 1}$		$C_{\tau 2}$	$C_{\tau 3}$	A_1	A_2
-4		13	-2	1.25	1000

$C_{\varepsilon 1}$, $C_{\varepsilon 2}$, $D_{k,eff}$ and $D_{\varepsilon,eff}$ are the same as in RNGkEpsilon model. The appropriate turbulence boundary conditions at the walls are $\partial k / \partial \hat{n}|_{wall} = 0$ and $\partial \varepsilon / \partial \hat{n}|_{wall} = 0$, where \hat{n} is the unit vector normal to the wall.

APPENDIX A. MODELING

The k and ε equations in the original model [6] follow the same formulations as the standard $k - \varepsilon$ model. The production term is found through $P_k = \tau_{ij}U_{i,j}$, while the shear stress formulation, τ_{ij} includes non-linear terms as [6]

$$\frac{\tau_{ij}}{\rho} = \nu_t (U_{i,j} + U_{j,i}) + T_{ij} - \frac{2}{3}k\delta_{ij}$$

$$T_{ij} = \frac{k^3}{(A_2 + \eta^3)\varepsilon^2} [C_{\tau 1}(U_{i,k}U_{k,j} + U_{j,k}U_{k,i} - \frac{2}{3}\Pi\delta_{ij})]$$

$$+ C_{\tau 2}(U_{i,k}U_{j,k} - \frac{1}{3}\tilde{\Pi}\delta_{ij}) + C_{\tau 3}(U_{k,i}U_{k,j} - \frac{1}{3}\tilde{\Pi}\delta_{ij})$$

ν_t	C_μ	η	Π	$\tilde{\Pi}$
$C_\mu \left(\frac{k^2}{\varepsilon}\right)$	$\left(\frac{2/3}{A_1 + \eta + \gamma\xi}\right)$	$\frac{k}{\varepsilon}S$	$U_{k,i}U_{i,k}$	$U_{k,i}U_{k,i}$
S	ξ	Ω	Ω_{ij}^*	γ
$\sqrt{2S_{ij}S_{ij}}$	$\left(\frac{k\Omega}{\varepsilon}\right)$	$(2\Omega_{ij}^*\Omega_{ij}^*)^{1/2}$	$(U_{i,j} - U_{j,i})/2 + 4\varepsilon_{mji}\omega_m$	0.9
$C_{\tau 1}$	$C_{\tau 2}$	$C_{\tau 3}$	A_1	A_2
-4	13	-2	1.25	1000

Here ω_m is the rotation rate of the reference frame which is NOT included in OpenFOAM. Other definitions and coefficients are the same as the standard $k - \varepsilon$ model.

A.1.7 LienCubicKE

The LienCubicKE model is the high-Re $k - \varepsilon$ model with wall functions developed by Lien et. al. [7]. The model includes third-order terms to account for the streamline curvature effects. The implementation of this model in the code follows the same formulation as the Non-linearKEShih model, with inclusion of higher order terms (C_4) in the non-linear stress tensor, (T_{ij}), as well as an extra term, ($C_{5\mu}$), in computation of C_μ . The appropriate turbulence boundary conditions at the walls are $\partial k / \partial \hat{n}|_{wall} = 0$ and $\partial \varepsilon / \partial \hat{n}|_{wall} = 0$, where \hat{n} is the unit vector normal to the wall.

T_{ij}								
symm	$\frac{k^3}{\varepsilon^2}$	$\frac{C_{\tau 1}}{f_\eta} ((U_{i,k} \cdot U_{k,j} + U_{k,i} \cdot U_{j,k})) + \frac{C_{\tau 2}}{f_\eta} ((U_{i,k} \cdot U_{j,k})) + \frac{C_{\tau 3}}{f_\eta} (U_{k,i} \cdot U_{k,j})$	$+ C_4$					
C_4								
$-20\frac{k^4}{\varepsilon^3}C_\mu^3 [(U_{i,k} \cdot U_{k,j}) \cdot U_{i,j} + (U_{i,k} \cdot U_{j,k}) \cdot U_{i,j} - (U_{k,i} \cdot U_{k,j}) \cdot U_{j,i} - (U_{k,i} \cdot U_{j,k}) \cdot U_{j,i}]$								
$C_{\tau 1}$	$C_{\tau 2}$	$C_{\tau 3}$	ν_t	$C_{5\mu}$				
-4	13	-2	$C_\mu \left(\frac{k^2}{\varepsilon} \right) + C_{5\mu}$	$-2C_\mu^3 \left(\frac{k^4}{\varepsilon^3} \right) (U_{i,j} + U_{j,i} ^2 - U_{i,j} - U_{j,i} ^2)$				

Other parameters and definitions are the same as in Nonlinear-KEShih model.

The original model is based on the standard $k - \varepsilon$ model, and a relation between stresses and strains as [7]

$$\begin{aligned} \frac{\overline{u'_i u'_j}}{k} &= \frac{2}{3} \delta_{ij} - \frac{\nu_T}{k} S_{ij} + C_1 \frac{\nu_T}{\varepsilon} \left[S_{ik} S_{kj} - \frac{1}{3} \delta_{ij} S_{kl} S_{kl} \right] \\ &+ C_2 \frac{\nu_T}{\varepsilon} [\Omega_{ik} S_{kj} + \Omega_{jk} S_{ki}] + C_3 \frac{\nu_T}{\varepsilon} \left[\Omega_{ik} \Omega_{jk} - \frac{1}{3} \delta_{ij} \Omega_{kl} \Omega_{kl} \right] \\ &+ C_4 \frac{\nu_T k}{\varepsilon^2} (S_{ki} \Omega_{lj} + S_{kj} \Omega_{li}) S_{kl} + C_5 \frac{\nu_T k}{\varepsilon^2} (S_{kl} S_{kl} - \Omega_{kl} \Omega_{kl}) S_{ij} \end{aligned}$$

C_μ	C_1	C_2	C_3	C_4	C_5
$\frac{2/3}{1.25+S+0.9\Omega}$	$\frac{3/4}{1000+S^3}$	$\frac{15/4}{1000+S^3}$	$\frac{19/4}{1000+S^3}$	$-10C_\mu^2$	$-2C_\mu^2$
A_1	A_2	S	Ω	S_{ij}	Ω_{ij}
1.25	1000	$\frac{k}{\varepsilon} \sqrt{\frac{1}{2} S_{ij} S_{ij}}$	$\frac{k}{\varepsilon} \sqrt{\frac{1}{2} \Omega_{ij} \Omega_{ij}}$	$\frac{\partial u_i}{\partial x_j} + \frac{\partial u_j}{\partial x_i}$	$\frac{\partial u_i}{\partial x_j} - \frac{\partial u_j}{\partial x_i}$

A.1.8 QZeta

The QZeta model is the two-equation $Q - \zeta$ low-Re turbulence model developed by Gibson and Dafa'Alla' [8]. The model uses the square root of the turbulent kinetic energy, $q = \sqrt{k}$, and its rate of dissipation, $\zeta = \tilde{\varepsilon}/2q$, where $\tilde{\varepsilon}$ is the isotropic dissipation rate $\tilde{\varepsilon} = \varepsilon - 2\nu(\partial \sqrt{k}/\partial x_j)$. The implementation of the model in OpenFOAM reads

$$\begin{aligned} \frac{\partial q}{\partial t} + \nabla \cdot (U q) - \nabla \cdot D_{q,eff} \nabla q &= G - \zeta \\ \frac{\partial \zeta}{\partial t} + \nabla \cdot (U \zeta) - \nabla \cdot D_{\zeta,eff} \nabla \zeta &= (2C_{\varepsilon 1} - 1)G \frac{\zeta}{q} - (2C_{\varepsilon 2} - 1)f_2 \frac{\zeta^2}{q} + E \end{aligned}$$

APPENDIX A. MODELING

q	ζ	ν_t	G	E	R_t	f_2
\sqrt{k}	$\left(\frac{\varepsilon}{2q}\right)$	$C_\mu f_\mu \left(\frac{k^2}{\varepsilon}\right)$	$\frac{\nu_t(2 S_{ij} ^2)}{2q}$	$\left(\frac{\nu_t \nu}{q}\right) \nabla(\nabla U) ^2$	$\left(\frac{qk}{2\nu\zeta}\right)$	$1 - 0.3e^{(-R_t^2)}$
$D_{q,eff}$	$D_{\zeta,eff}$	$C_{\varepsilon 1}$	$C_{\varepsilon 2}$	C_μ	α_q	α_ζ
$\nu + \alpha_q \nu_t$	$\nu + \alpha_\zeta \nu_t$	1.44	1.92	0.09	1	0.76923

The model works for both isotropic and anisotropic turbulence, and the coefficient f_μ is then found through

$$f_\mu = \begin{cases} e^{\frac{(-2.5+R_t/20)}{(1+R_t/130)^3}} & \text{for anisotropic model} \\ e^{\frac{-6}{(1+R_t/50)}} (1 + 3e^{-R_t/10}) & \text{for isotropic model} \end{cases}$$

The appropriate turbulence boundary conditions at the walls are $\partial q / \partial \hat{n}|_{wall} = 0$ and $\partial \zeta / \partial \hat{n}|_{wall} = 0$, where \hat{n} is the unit vector normal to the wall.

The original model for the isotropic turbulence reads [8]

$$\begin{aligned} \frac{Dq}{Dt} &= \frac{\partial}{\partial x_j} \left(\left(\nu + \frac{\nu_t}{\sigma_q} \right) \frac{\partial q}{\partial x_j} \right) + Q - \zeta \\ \frac{D\zeta}{Dt} &= \frac{\partial}{\partial x_j} \left(\left(\nu + \frac{\nu_t}{\sigma_\zeta} \right) \frac{\partial \zeta}{\partial x_j} \right) + \frac{\zeta}{q} (C_{\zeta 1} f_{\zeta 1} Q - C_{\zeta 2} f_{\zeta 2} \zeta) + \Psi \end{aligned}$$

$Q = \frac{P}{2q}$	Ψ	γ_t	Re_τ
$\gamma_t \frac{\partial U_i}{\partial x_j} \left(\frac{\partial U_i}{\partial x_j} + \frac{\partial U_j}{\partial x_i} \right)$	$2\nu \gamma_t \left(\frac{\partial^2 U_i}{\partial x_k \partial x_m} \right) \left(\frac{\partial^2 U_i}{\partial x_k \partial x_m} \right)$	$\frac{C_\mu f_\mu}{4} \left(\frac{q^2}{\zeta} \right)$	$\left(\frac{q^3}{2\nu\zeta} \right)$
$C_{\zeta 1} f_{\zeta 1}$	$C_{\zeta 2} f_{\zeta 2}$	$f_{\varepsilon 1}$	$f_{\varepsilon 2}$
$2C_{\varepsilon 1} f_{\varepsilon 1} - 1$	$2C_{\varepsilon 2} f_{\varepsilon 2} - 1$	1.0	$1 - 0.3e^{(-Re_\tau^2)}$
f_μ	ν_t	σ_q	σ_ζ
$e^{\frac{-6.0}{(1+Re_\tau/50)^2}} \left[1 + 3e^{-\frac{Re_\tau}{10}} \right]$	$2q\gamma_t \equiv C_\mu f_\mu \frac{q^3}{2\zeta}$	1	1.3

The model constants $C_{\varepsilon 1}$, $C_{\varepsilon 2}$ and C_μ are the same as in the original $k - \varepsilon$ model.

A.1.9 LaunderSharmaKE

The LaunderSharmaKE model is the low-Re $k - \varepsilon$ model developed by Launder and Sharma [9]. The model is implemented in OpenFOAM as

$$\frac{\partial k}{\partial t} + \nabla \cdot (Uk) - \nabla \cdot D_{k,eff} \nabla k = G - (\tilde{\varepsilon} + D)$$

$$\frac{\partial \tilde{\varepsilon}}{\partial t} + \nabla \cdot (U\tilde{\varepsilon}) - \nabla \cdot D_{\varepsilon,eff} \nabla \tilde{\varepsilon} = C_{\varepsilon 1} G \frac{\tilde{\varepsilon}}{k} - C_{\varepsilon 2} f_2 \frac{\tilde{\varepsilon}^2}{k} + E$$

ν_t	E	D	f_μ	f_2
$C_\mu f_\mu \frac{k^2}{\tilde{\varepsilon}}$	$2\nu\nu_t \nabla \nabla U ^2$	$2\nu \nabla \sqrt{k} ^2$	$e^{\left(\frac{-3.4}{(1+\frac{k^2}{50\nu\varepsilon})^2}\right)}$	$1 - 0.3e^{-\min\left(\left(\frac{k^2}{\nu\varepsilon}\right)^2, 50\right)}$

Other coefficients are identical to the kEpsilon model. For OpenFOAM-1.5.x users it is worth noting that `epsilon` in the time directories is the same as $\tilde{\varepsilon}$ (i.e. not ε). The appropriate turbulence boundary conditions at the walls are $k_{wall} = 0$ and $\tilde{\varepsilon}_{wall} = 0$.

The original model reads [9]

$$\frac{Dk}{Dt} = \frac{\partial}{\partial x_j} \left[\left(\nu + \frac{\nu_t}{\sigma_k} \right) \frac{\partial k}{\partial x_j} \right] + P_k - \tilde{\varepsilon} - D$$

$$\frac{D\tilde{\varepsilon}}{Dt} = \frac{\partial}{\partial x_j} \left[\left(\nu + \frac{\nu_t}{\sigma_\varepsilon} \right) \frac{\partial \tilde{\varepsilon}}{\partial x_j} \right] + C_{\varepsilon 1} f_1 \frac{\tilde{\varepsilon}}{k} P_k - C_{\varepsilon 2} f_2 \frac{\tilde{\varepsilon}^2}{k} + E$$

$\tilde{\varepsilon}$	D	E	f_μ	f_1	f_2
$\varepsilon - D$	$2\nu \left(\frac{\partial \sqrt{k}}{\partial x_j} \right)^2$	$2\nu\nu_t \left(\frac{\partial^2 U_i}{\partial x_j \partial x_k} \right)^2$	$e^{\left(\frac{-3.4}{(1+R_T/50)^2}\right)}$	1	$1 - 0.3e^{(-R_T^2)}$
R_T	c_μ	$c_{\varepsilon 1}$	$c_{\varepsilon 2}$	σ_k	σ_ε
$\left(\frac{k^2}{\nu\varepsilon}\right)$	0.09	1.44	0.92	1.0	1.22

A.1.10 LamBremhorstKE

The LamBremhorstKE model is the low-Re Lam-Bremhorst $k-\varepsilon$ model [10]. The implementation in OpenFOAM reads

$$\frac{\partial k}{\partial t} + \nabla \cdot (Uk) - \nabla \cdot D_{k,eff} \nabla k = G - \varepsilon$$

$$\frac{\partial \varepsilon}{\partial t} + \nabla \cdot (U\varepsilon) - \nabla \cdot D_{\varepsilon,eff} \nabla \varepsilon = C_{\varepsilon 1} f_1 G \frac{\varepsilon}{k} - C_{\varepsilon 2} f_2 \frac{\varepsilon^2}{k}$$

Other coefficients are the same as in the kEpsilon model. The appropriate turbulence boundary conditions at the walls are $k_{wall} = 0$ and $\partial\varepsilon/\partial\hat{n}|_{wall} = 0$, where \hat{n} is the unit vector normal to the wall.

APPENDIX A. MODELING

G	ν_t	R_t	f_μ
$\nu_t 2 S_{ij} ^2$	$C_\mu f_\mu \left(\frac{k^2}{\varepsilon}\right)$	$\left(\frac{k^2}{\nu\varepsilon}\right)$	$\left(1 - e^{-0.0165\sqrt{k}\frac{y}{\nu}}\right)^2 \left(1 + \frac{20.5}{R_t}\right)$

The k and ε equations, as well as the ν_t formulation of the original model follow those of the Launder-Sharma $k - \varepsilon$ model. The model coefficients are [10]

f_μ	f_1	f_2	Re_n	Re_t
$\left[1 - e^{(-0.0165Re_n)}\right]^2 \left(1 + \frac{20.5}{Re_t}\right)$	$1 + \left(\frac{0.05}{f_\mu}\right)^3$	$1 - e^{-Re_t^2}$	$\left(\frac{\sqrt{k}Y_n}{\nu}\right)$	$\left(\frac{k^2}{\nu\varepsilon}\right)$

Where Y_n is the distance to the nearest wall. Other model coefficients are the same as in the standard $k - \varepsilon$ model.

A.1.11 LienLeschzinerLowRe

The LienLeschzinerLowRe model is the low-Re $k - \varepsilon$ model developed by Lien and Leschziner [11]. The model is implemented in OpenFOAM as

$$\begin{aligned} \frac{\partial k}{\partial t} + \nabla \cdot (Uk) - \nabla \cdot D_{k,eff} \nabla k &= G - \varepsilon \\ \frac{\partial \varepsilon}{\partial t} + \nabla \cdot (U\varepsilon) - \nabla \cdot D_{\varepsilon,eff} \nabla \varepsilon &= C_{\varepsilon 1} G \frac{\varepsilon}{k} + C_{\varepsilon 2} f_2 C_\mu^{0.75} k^{0.5} \frac{e^{-A_\mu y^*}}{\kappa y (1 - e^{-A_\varepsilon y^*})} \varepsilon - C_{\varepsilon 2} f_2 \frac{\varepsilon^2}{k} \end{aligned}$$

y^*	ν_t	f_μ	S_2	A_m
$\left(\frac{\sqrt{k}}{\nu}\right) y$	$C_\mu f_\mu \left(\frac{k^2}{\varepsilon}\right)$	$\left(\frac{1-e^{(-A_m y^*)}}{1-e^{(-A_\varepsilon y^*)}}\right)$	$S_{ij} : U_{i,j}$	0.016
f_2	R_t	G	A_ε	A_μ
$1 - 0.3e^{(-R_t^2)}$	$\left(\frac{k^2}{\nu\varepsilon}\right)$	$C_\mu f_\mu \left(\frac{k^2}{\varepsilon}\right) S_2$	0.263	0.00222

The definitions of C_μ , α_k , α_ε , $C_{\varepsilon 1}$, $C_{\varepsilon 2}$, $D_{k,eff}$ and $D_{\varepsilon,eff}$ are the same as in the kEpsilon model. The appropriate turbulence boundary conditions at the walls are $k_{wall} = 0$ and $\partial \varepsilon / \partial \hat{n}|_{wall} = 0$, where \hat{n} is the unit vector normal to the wall.

The original model [11] reads

$$\frac{Dk}{Dt} = \frac{\partial}{\partial x_i} \left[\left(\nu + \frac{\nu_t}{\sigma_k} \right) \frac{\partial k}{\partial x_i} \right] + P_k - \varepsilon$$

$$\frac{D\varepsilon}{Dt} = \frac{\partial}{\partial x_i} \left[\left(\nu + \frac{\nu_t}{\sigma_\varepsilon} \right) \frac{\partial \varepsilon}{\partial x_i} \right] + C_{\varepsilon 1} f_1 \frac{\varepsilon}{k} P_k - C_{\varepsilon 2} f_2 \frac{\varepsilon^2}{k}$$

f_μ	f_1	f_2	ν_t
$\frac{1-e^{(-0.016y^*)}}{(1-e^{-0.263y^*})}$	$1 + \frac{P'_k}{P_k}$	$1 - 0.3e^{-R_T^2}$	$C_\mu f_\mu \left(\frac{k^2}{\varepsilon} \right)$
y^*	R_T	P'_k	
$y \left(\frac{\sqrt{k}}{\nu} \right)$	$\frac{k^2}{\nu \varepsilon}$	$\left(\frac{1.92[1-0.3e^{(-R_T^2)}]k^{3/2}}{3.53y[1-e^{(-0.263y^*)}]} \right) e^{-0.00222y^{*2}}$	

$C_{1_\varepsilon}, C_{2_\varepsilon}, C_\mu, \sigma_k, \sigma_\varepsilon, S$ and S_{ij} are the same as in the standard $k - \varepsilon$ model.

A.1.12 LienCubicKELowRe

The LienCubicKELowRe model is the low-Re variant of the LienCubicKE $k - \varepsilon$ model [12]. The model is implemented in OpenFOAM as

$$\frac{\partial k}{\partial t} + \nabla \cdot (Uk) - \nabla \cdot D_{k,eff} \nabla k = G - \varepsilon$$

$$\frac{\partial \varepsilon}{\partial t} + \nabla \cdot (U\varepsilon) - \nabla \cdot D_\varepsilon \nabla \varepsilon = C_{\varepsilon 1} G \frac{\varepsilon}{k} + \frac{C_{\varepsilon 2} f_2 C_\mu^{0.75} k^{0.5}}{\kappa y (1 - e^{-A_\varepsilon y^*})} \cdot e^{-A_\mu y^{*2}} \varepsilon - C_{\varepsilon 2} f_2 \frac{\varepsilon^2}{k}$$

where the non-linear stress tensor, T_{ij} is computed through

$$T_{ij} = symm \left[\frac{k^3}{\varepsilon^2} \left[\frac{C_{\tau 1}}{f_\eta} ((U_{i,k} \cdot U_{k,j} + U_{k,i} \cdot U_{j,k})) + \frac{C_{\tau 2}}{f_\eta} ((U_{i,k} \cdot U_{j,k})) \right. \right.$$

$$\left. \left. + \frac{C_{\tau 3}}{f_\eta} (U_{k,i} \cdot U_{k,j}) \right] - 20 \frac{k^4}{\varepsilon^3} C_\mu^3 ((U_{i,k} \cdot U_{k,j}) \cdot U_{i,j} + (U_{i,k} \cdot U_{j,k}) \cdot U_{i,j} \right.$$

$$\left. - (U_{k,i} \cdot U_{k,j}) \cdot U_{j,i} - (U_{k,i} \cdot U_{j,k}) \cdot U_{j,i} \right] + min(C_{5\mu}, 0) U_{i,k} \right]$$

The definitions of $G, C_\mu, \alpha_k, \alpha_\varepsilon, C_{\varepsilon 1}, C_{\varepsilon 2}, D_{k,eff}, D_{\varepsilon,eff}, C_{\tau 1}, C_{\tau 2}, C_{\tau 3}, \eta, \xi, C_{5\mu}$ and f_η are the same as in LienCubicKE model. The appropriate turbulence boundary conditions at the walls are $k_{wall} = 0$ and $\partial \varepsilon / \partial \hat{n}|_{wall} = 0$, where \hat{n} is the unit vector normal to the wall.

APPENDIX A. MODELING

	ν_t	f_2
C_μ	$\frac{1-e^{(-A_m y^*)}}{1-e^{(-A_\varepsilon y^*)}}$	$\frac{k^2}{\varepsilon} + \max(0, C_{5\mu})$
R_t	y^*	A_m
$\left(\frac{k^2}{\nu\varepsilon}\right)$	$\left(\frac{\sqrt{k}}{\nu}\right) y$	0.016
		0.00222
		0.263

The transport equation for ε in the original model [12] is the same as in the Lien-Leschziner $k - \varepsilon$ model. The transport equation for the Reynolds stresses read

$$\begin{aligned} \frac{\overline{u'_i u'_j}}{k} &= \frac{2}{3} \delta_{ij} - \frac{\nu_T}{k} S_{ij} + C_1 \frac{\nu_T}{\varepsilon} \left[S_{ik} S_{kj} - \frac{1}{3} \delta_{ij} S_{kl} S_{kl} \right] \\ &+ C_2 \frac{\nu_T}{\varepsilon} [\Omega_{ik} S_{kj} + \Omega_{jk} S_{ki}] + C_3 \frac{\nu_T}{\varepsilon} \left[\Omega_{ik} \Omega_{jk} - \frac{1}{3} \delta_{ij} \Omega_{kl} \Omega_{kl} \right] \\ &+ C_4 \frac{\nu_T k}{\varepsilon^2} (S_{ki} \Omega_{lj} + S_{kj} \Omega_{li}) S_{kl} + C_5 \frac{\nu_T k}{\varepsilon^2} (S_{kl} S_{kl} - \Omega_{kl} \Omega_{kl}) S_{ij} \end{aligned}$$

C_1	C_2	C_3	C_4	C_5
$\frac{3/4}{1000+S^3}$	$\frac{15/4}{1000+S^3}$	$\frac{19/4}{1000+S^3}$	$-10C_\mu^2$	$-2C_\mu^2$
S	Ω	S_{ij}	Ω_{ij}	ν_T
$\frac{k}{\varepsilon} \sqrt{\frac{1}{2} S_{ij} S_{ij}}$	$\frac{k}{\varepsilon} \sqrt{\frac{1}{2} \Omega_{ij} \Omega_{ij}}$	$\frac{\partial u_i}{\partial x_j} + \frac{\partial u_j}{\partial x_i}$	$\frac{\partial u_i}{\partial x_j} - \frac{\partial u_j}{\partial x_i}$	$f_\mu C_\mu \frac{k^2}{\varepsilon}$
f_μ	y^*	f_1	f_2	
$(1 - e^{-0.0198y^*}) \left(1 + \frac{5.29}{y^*}\right)$	$y \frac{\sqrt{k}}{\nu}$	$1 + \frac{P'_k}{P_k}$	$1 - 0.3^{-R_T^2}$	
P'_k		R_T	C_μ	
$1.33 \left(1 - 0.3^{-R_T^2}\right) \left(P_k + 2\nu \frac{k}{y^2}\right) e^{-0.00375y^{*2}}$		$\frac{k^2}{\nu\varepsilon}$	$\frac{2/3}{1.25+S+0.9\Omega}$	

The model coefficients $C_{\varepsilon 1}$, $C_{\varepsilon 2}$ and C_μ are the same as standard $k - \varepsilon$ model.

A.1.13 LRR

The LRR model is the high-Re Reynolds Stress Transport Model (RSTM) developed by Launder, Reece and Rodi with wall functions [13]. The model solves transport equations of the Reynolds stresses, $\overline{u_i u_j}$, and the turbulence dissipation rate, ε . The turbulent kinetic energy, k , is then found through $k = \sqrt{\overline{u_i^2} + \overline{u_j^2} + \overline{u_k^2}}$. The model is implemented in OpenFOAM as

$$\begin{aligned} \frac{\partial R}{\partial t} + \nabla \cdot (UR) - (\nabla \cdot U)R - \nabla \cdot (D_{R,eff} \nabla R) + (C_{lrr,1} \frac{\varepsilon}{k} R) = \\ P - \frac{2}{3}(1 - C_{lrr,1})I\varepsilon - C_{lrr,2} dev(P) \\ \frac{\partial \varepsilon}{\partial t} + \nabla \cdot (U\varepsilon) - (\nabla \cdot U)\varepsilon - \nabla \cdot (D_{\varepsilon,eff} \nabla \varepsilon) = C_{\varepsilon 1}G \frac{\varepsilon}{k} - C_{\varepsilon 2} \frac{\varepsilon^2}{k} \end{aligned}$$

P	R	G	k	$D_{R,eff}$
$-2symm(R \cdot U_{i,j})$	$\overline{u_i u_j}$	$\frac{1}{2} tr(P) $	$\frac{1}{2}tr(R)$	$\nu + \alpha_R \nu_t$
α_R	ν_t	$C_{lrr,1}$	$C_{lrr,2}$	C_s
1	$C_\mu \left(\frac{k^2}{\varepsilon} \right)$	1.8	0.6	0.25

The definitions of C_μ , α_ε , $C_{\varepsilon 1}$, $C_{\varepsilon 2}$ and $D_{\varepsilon,eff}$ are the same as in the kEpsilon model. The appropriate turbulence boundary conditions at the walls are $\partial R / \partial \hat{n}|_{wall} = 0$ and $\partial \varepsilon / \partial \hat{n}|_{wall} = 0$, where \hat{n} is the unit vector normal to the wall.

The original model is developed as a low-Re model and thus includes near wall corrections in the $\overline{u_i u_j}$ equations. The transport equations in the original model read [13]

$$\begin{aligned} \frac{D(\overline{u_i u_j})}{Dt} = & - \left[\overline{u_j u_k} \frac{\partial U_i}{\partial x_k} + \overline{u_i u_k} \frac{\partial U_j}{\partial x_k} \right] - \frac{2}{3} \delta_{ij} \varepsilon \\ & - C_{\varepsilon 1} \frac{\varepsilon}{k} (\overline{u_i u_j} - \frac{2}{3} \delta_{ij} k) + (\phi_{ij} + \phi_{ji})_2 + (\phi_{ij} + \phi_{ji})_w \\ & + C_s \frac{\partial}{\partial x_k} \frac{k}{\varepsilon} \left[\overline{u_i u_l} \frac{\partial \overline{u_j u_k}}{\partial x_l} + \overline{u_j u_l} \frac{\partial \overline{u_k u_i}}{\partial x_l} + \overline{u_k u_l} \frac{\partial \overline{u_i u_j}}{\partial x_l} \right] \\ \frac{D\varepsilon}{Dt} = & C_\varepsilon \frac{\partial}{\partial x_k} \left(\frac{k}{\varepsilon} \overline{u_k u_l} \frac{\partial \varepsilon}{\partial x_l} \right) - C_{\varepsilon 1} \frac{\varepsilon \overline{u_i u_k}}{k} \frac{\partial U_i}{\partial x_k} - C_{\varepsilon 2} \frac{\varepsilon^2}{k} \end{aligned}$$

$(\phi_{ij} + \phi_{ji})_w$	P
$[0.125 \frac{\varepsilon}{k} (\overline{u_i u_j} - \frac{2}{3} k \delta_{ij}) + 0.015 (P_{ij} - D_{ij})] \left(\frac{k^{\frac{3}{2}}}{\varepsilon x_2} \right)$	$-2 \overline{u_i u_j} \frac{\partial U_i}{\partial x_j}$
$(\phi_{ij} + \phi_{ji})_2$	P_{ij}
$-\gamma (P_{ij} - \frac{2}{3} P \delta_{ij})$	$- \left[\overline{u_i u_k} \frac{\partial U_j}{\partial x_k} + \overline{u_j u_k} \frac{\partial U_i}{\partial x_k} \right] - \left[\overline{u_i u_k} \frac{\partial U_k}{\partial x_j} + \overline{u_j u_k} \frac{\partial U_k}{\partial x_i} \right]$

Here P is the production rate and x_2 is the normal distance of the cell to the surface. The coefficients $C_{\varepsilon 1}$ and $C_{\varepsilon 2}$ are the same as in the standard $k - \varepsilon$ model.

APPENDIX A. MODELING

A.1.14 LaunderGibsonRSTM

The LaunderGibsonRSTM model is the Reynolds Stress Transport Model with wall-reflection terms developed by Launder and Gibson [14]. The model is implemented in OpenFOAM as

$$\begin{aligned} \frac{\partial R}{\partial t} + \nabla \cdot (UR) - (\nabla \cdot U)R - \nabla \cdot (D_{R,eff} \nabla R) + (C_{lg,1} \frac{\varepsilon}{k} R) = \\ P + \frac{2}{3}(C_{lg,1} - 1)I\varepsilon - C_{lg,2}dev(P) + reflection_{wall} \\ \frac{\partial \varepsilon}{\partial t} + \nabla \cdot (U\varepsilon) - (\nabla \cdot U)\varepsilon - \nabla \cdot (D_{\varepsilon,eff} \nabla \varepsilon) = C_{\varepsilon 1}G \frac{\varepsilon}{k} - C_{\varepsilon 2} \frac{\varepsilon^2}{k} \end{aligned}$$

reflection _{wall}							
symm(I(y _n · reflect) · y _n - 1.5(y _n (reflect · y _n) + (y _n · reflect)y _n)) (C _μ ^{0.75} k ^{1.5} / κyε)							
reflect				P			
C _{1,ref} ε/k R - C _{2,ref} C _{lg,2} dev(P)				-2symm(R · U _{i,j})			
G	k	C _{lg,1}	C _{lg,2}	C _{1,ref}	C _{2,ref}	C _ε	α _R
1/2 tr(P)	1/2tr(R)	1.8	0.6	0.5	0.3	0.15	1.22

C_μ, α_ε, C_{ε1}, C_{ε2}, D_{R,eff} and D_{ε,eff} are the same as in the LRR model. The turbulence boundary conditions at the walls are k_{wall} = 0 and ∂ε/∂n̂|_{wall} = 0.

The original model [14] reads

$$\begin{aligned} \frac{D(\overline{u'_i u'_j})}{Dt} &= D \overline{\frac{u'_i u'_j}{u'_i u'_j}} + P_{ij} + \Phi_{ij} - \frac{2}{3} \delta_{ij} \varepsilon \\ \frac{D\varepsilon}{Dt} &= D_\varepsilon + \frac{\varepsilon}{k} (0.5C_{\varepsilon 1}P_{kk} - C_{\varepsilon 2}\varepsilon) \end{aligned}$$

ϕ_{ij}	$\phi_{ij,1}$	$\phi_{ij,2}$
$\phi_{ij,1} + \phi_{ij+2} + \phi'_{ij,1} + \phi'_{ij,2}$	$-C_{\varepsilon 1} \frac{\varepsilon}{k} \left(\overline{u'_i u'_j} - \frac{2}{3} \delta_{ij} k \right)$	$-C_{\varepsilon 2} \left(P_{ij} - \frac{1}{3} \delta_{ij} P \right)$
$\phi'_{ij,1}$		P_{ij}
$C'_{\varepsilon 1} \frac{\varepsilon}{k} \left(\overline{u'_k u'_m} n_k n_m \delta_{ij} - \frac{3}{2} \overline{u'_k u'_i} n_k n_j - \frac{3}{2} \overline{u'_k u'_j} n_k n_i \right) f$		$- \left(\overline{u'_j u'_k} \frac{\partial u_i}{\partial x_k} + \overline{u'_i u'_k} \frac{\partial u_j}{\partial x_k} \right)$
$\phi'_{ij,2}$		$\tilde{\phi}_{ij}$
$C'_{\varepsilon 2} \left(\tilde{\phi}_{km} n_k n_m \delta_{ij} - \frac{3}{2} \tilde{\phi}_{ik} n_k n_j - \frac{3}{2} \tilde{\phi}_{jk} n_k n_i \right) f$		$P_{ij} - \frac{1}{3} \delta_{ij} P_{kk}$
$D_{\overline{u'_i u'_j}}$	D_ε	f
$\frac{\partial}{\partial x_k} \left(C_s \frac{k \overline{u'_k u'_l}}{\varepsilon} \frac{\partial u'_i u'_j}{\partial x_l} \right)$	$\frac{\partial}{\partial x_k} \left(C_\varepsilon \frac{k \overline{u'_k u'_l}}{\varepsilon} \frac{\partial \varepsilon}{\partial x_l} \right)$	$\left(\frac{C_\mu^{0.75} k^{1.5}}{\kappa y \varepsilon} \right)$
$C_{\varepsilon 1}$	$C_{\varepsilon 2}$	C'_1
1.8	0.6	0.5
		C'_2
		C_s
		C_ε
		0.18
		0.22
		0.18

C_μ , $C_{\varepsilon 1}$ and $C_{\varepsilon 2}$ are the same as in the standard $k - \varepsilon$ model.

A.1.15 SpalartAllmaras

The SpalartAllmaras model is the 1-equation mixing-length model developed for external flows by Spalart and Allmaras [15]. The model solves a transport equation for the turbulent viscosity, $\tilde{\nu}$ (Spalart-Allmaras variable). The implementation of this model in OpenFOAM is done as

$$\frac{d\tilde{\nu}}{dt} + \nabla \cdot (U \tilde{\nu}) - (\nabla \cdot U) \tilde{\nu} - \nabla \cdot (D_{\tilde{\nu},eff} \nabla \tilde{\nu}) - \alpha_\nu C_{b2} |\nabla \tilde{\nu}|^2 = C_{b1} \tilde{S} \tilde{\nu} - C_{w1} f_w \frac{\tilde{\nu}^2}{d^2}$$

\tilde{S}	g	r
$f_{v3} \sqrt{2} \Omega + f_{v2} \left(\frac{\tilde{\nu}}{(\kappa d)^2} \right)$	$r + C_{\omega 2} (r^6 - r)$	$\min \left(\left(\frac{\tilde{\nu}}{\tilde{S} \kappa^2 d^2} \right), 10 \right)$
f_{v1}	f_{v2}	f_{v3}
$\left(\frac{\chi^3}{\chi^3 + C_{v1}^3} \right)$	$1 - \frac{\chi}{1 + \chi f_{v1}}$	$\left(\frac{1 + \chi f_{v1}}{C_{v2}} \right) \left(\frac{3(1 + \chi/C_{v2} + (\chi/C_{v2})^2)}{(1 + \chi/C_{v2})^3} \right)$
ν_t	χ	f_{t2}
$\tilde{\nu} f_{v1}$	$\left(\frac{\tilde{\nu}}{\nu} \right)$	$C_{t3} e^{-c_{t4} \chi^2}$
$D_{\tilde{\nu},eff}$	$C_{\omega 1}$	$C_{\omega 2}$
$\nu + \alpha_\nu \tilde{\nu}$	$\frac{(C_{b1})}{(\kappa^2)} + \alpha_\nu (1 + C_{b2})$	$C_{\omega 3}$
κ	C_{v1}	C_{v2}
0.41	7.1	5
		C_{t3}
		1.1
		2

Here d is the distance to the closest surface. The appropriate boundary condition at the walls is $\tilde{\nu}_{wall} = 0$.

The original model [15] calculates the turbulent viscosity through

$$\frac{D\tilde{\nu}}{Dt} = C_{b1}(1-f_{t2})\tilde{S}\tilde{\nu} - \left[c_{\omega 1}f_{\omega} - \frac{c_{b1}}{\kappa^2}f_{t2} \right] \left(\frac{\tilde{\nu}}{d} \right)^2 + \frac{1}{\sigma} \left[\frac{\partial}{\partial x_j} \left((\nu + \tilde{\nu}) \frac{\partial \tilde{\nu}}{\partial x_j} \right) + c_{b2} \frac{\partial \tilde{\nu}}{\partial x_i} \frac{\partial \tilde{\nu}}{\partial x_i} \right]$$

\tilde{S}	f_{v2}	f_{v3}	σ
$f_{v3}\Omega + \left(\frac{\tilde{\nu}}{\kappa^2 d^2} \right) f_{v2}$	$\left[\frac{1}{(\chi/c_{v2})^3} \right]$	$\left(\frac{(1+\chi f_{v1})(1-f_{v2})}{\chi} \right)$	2/3

Other coefficients are the same as those implemented in OpenFOAM.

A.2 Wall Functions

Wall functions are used when the centers of the wall-adjacent cells are in the overlap region of the boundary layer, i.e. within the range $30 < Y^+ < 100$. There are different wall function implementations for different turbulence models in OpenFOAM, which are described in the following sub-sections.

A.2.1 Linear $k - \varepsilon$ Models

Before applying the production term, G , in the k and ε equations, it is modified in the wall-adjacent cells according to

$$G = (\nu_{tw} + \nu_w) \text{abs} \left(\frac{\partial U}{\partial n} \Big|_{wall} \right) C_{\mu}^{0.25} \left(\frac{\sqrt{k}}{\kappa y} \right)$$

Further, before solving the equations, the dissipation, ε , is fixed in the wall-adjacent cells according to

$$\varepsilon = C_{\mu}^{0.75} \left(\frac{k^{1.5}}{\kappa y} \right)$$

ν_w	y^+
ν	$C_{\mu}^{0.25} y \left(\frac{\sqrt{k}}{\nu_w} \right)$

y is the distance from the wall. After computing k , ε and ν_t , the turbulent viscosity of the wall-adjacent cells is modified according to

$$\nu_{tw} = \nu_w \left(\frac{y^+ \kappa}{\log(Ey^+) - 1} \right) \quad (\text{A.1})$$

For the very fine cells near the wall, where $y^+ < y_{lam}^+$, the production term and the turbulent viscosity for the wall-adjacent cells become $G = 0$ and ν_t .

A.2.2 Non-linear $k - \varepsilon$ Models

For non-linear $k - \varepsilon$ models an extra non-linear term is added to the generation term

$$G = (\nu_{tw} + \nu_w) \operatorname{abs}\left(\frac{\partial U}{\partial n}|_{wall}\right) C_\mu^{0.25} \left(\frac{\sqrt{k}}{\kappa y} \right) - (T_{ij} : U_{i,j})$$

C_μ is a local variable in each cell, which is found in the descriptions of the non-linear turbulence models.

A.2.3 The kOmegaSST Model

The wall function formulation in the *kOmegaSST* model follows the same principles as those mentioned above, with the only difference being the frequency ω , which is computed instead of dissipation rate, ε

$$G = (\nu_{tw} + \nu_w) \operatorname{abs}\left(\frac{\partial U}{\partial n}|_{wall}\right) C_\mu^{0.25} \left(\frac{\sqrt{k}}{\kappa y} \right)$$

$$\omega = \frac{\sqrt{k}}{C_\mu^{0.25} \kappa y}$$

Other definitions are the same as in other models.

A.3 Numerical Methods

Three different numerical schemes are used in the computations: central differencing (*CD*), upwind differencing (*UD*) and Gamma. Figure A.1 shows three nodes *U*, *C* and *D*, in which the values of the general parameters ϕ_U , ϕ_C and ϕ_D are present. All interpolations must be based on the quantities which exist in the nodes. The velocity at face *f* is U_f . The goal of the numerical schemes is to find an appropriate estimation for the value ϕ_f at face *f*. In the following subsections each numerical scheme will be discussed briefly.

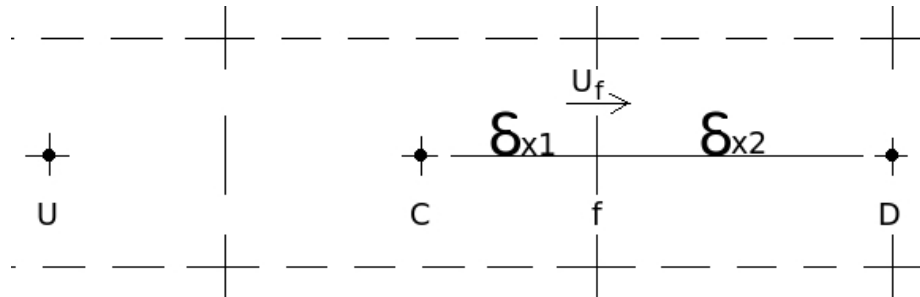


Figure A.1: Cells *U*, *C* and *D*, as well as face *f*.

A.3.1 Central Differencing, *CD*

In the central differencing method, a linear interpolation of the values ϕ_C and ϕ_D at two adjacent nodes *C* and *D* is exploited to estimate the value ϕ_f at the face *f*. The method is mathematically described as

$$\begin{aligned}\phi_f &= f_x \phi_C + (1 - f_x) \phi_D \\ f_x &= \frac{\delta_{x1}}{\delta_{x1} + \delta_{x2}}\end{aligned}\tag{A.2}$$

The central differencing scheme is a second-order accurate scheme.

A.3.2 Upwind Differencing, *UD*

In the upwind scheme, the value ϕ_f on the face *f* is estimated as

$$\phi_f = \begin{cases} \phi_C & \text{if } U_f > 0 \\ \phi_D & \text{otherwise} \end{cases}$$

The upwind scheme is first order accurate.

A.3.3 Gamma Differencing

The Gamma scheme is a blend of *CD* and *UD* [16]. The model has a constant β_m which can vary between 0.1 and 0.5. The blending factor γ and the normalized cell value ϕ_C are defined as

$$\begin{cases} \gamma = \frac{\tilde{\phi}_C}{\beta_m} \\ \tilde{\phi}_C = \frac{\phi_C - \phi_U}{\phi_D - \phi_U} \end{cases}$$

The Gamma scheme works then based on the values of γ and ϕ_C

$$\phi_f = \begin{cases} \phi_C & \text{if } \tilde{\phi}_C \leq 0 \text{ or } \phi_C \geq 1 \\ f_x \phi_C + (1 - f_x) \phi_D & \text{if } \beta_m \geq \tilde{\phi}_C \geq 1 \\ (1 - \gamma(1 - f_x)) \phi_C + \gamma(1 - f_x) \phi_D & \text{if } 0 \geq \tilde{\phi}_C \geq \beta_m \end{cases}$$

The Gamma scheme is second order accurate.

A.4 Frozen Rotor

The flow in the generator is simulated using the Frozen Rotor approach. This approach is based on a multiple reference frame method in which an inertial region and a rotating region are specified. The two regions are separated from each other by an axi-symmetric interface [17]. The rotating region is provided with extra source terms which account for the rotation. The rotor and the stator, thus, have a fixed position during the computations. The Navier-Stokes and continuity equations are based on convection of the absolute velocity \vec{u}_I and are given by

$$\frac{\partial \vec{u}_I}{\partial t} + \nabla \cdot (\vec{u}_R \otimes \vec{u}_I) + \vec{\Omega} \times \vec{u}_I = -\nabla(p/\rho) + \nu \nabla \cdot \nabla(\vec{u}_I)$$

$$\nabla \cdot \vec{u}_I = 0$$

Here \vec{u}_R is the velocity relative to the reference frame and $\vec{\Omega}$ is the rotation vector of the reference frame.

A.5 Forces and Torques on the Rotor

The rotor rotates in a viscous fluid. This means that in order to keep the rotational motion at a constant rotational speed, a certain torque should be applied to the rotor. The rotor torque should balance the torques exerted by the frictional forces and pressure forces on the rotor body, i.e.

$$\vec{T}_{rotor} = \vec{T}_{friction} + \vec{T}_{pressure}$$

The torque from frictional forces, $\vec{T}_{friction}$, is caused by the friction between the fluid and the solid body of the rotor, while the pressure torque, $\vec{T}_{pressure}$, is caused by the pressure acting normal to the rotor surface. The torque required to keep the rotation at a constant speed for each case can be used as a measure to determine the ventilation losses in the generator.

The forces and torques on the rotor are computed according to

$$\vec{F}_{pressure} = \sum_{rotor faces} (p \vec{A}_{face})$$

$$\vec{F}_{friction} = \sum_{rotor faces} (\vec{A}_{face} \cdot \tau_{viscous})$$

$$\vec{M}_{pressure} = \sum_{rotor faces} (\vec{X}_{face} \times (p \vec{A}_{face}))$$

$$\vec{M}_{friction} = \sum_{rotor faces} (\vec{X}_{face} \times (\vec{A}_{face} \cdot \tau_{viscous}))$$

Here $\vec{F}_{pressure}$ is the total pressure force, $\vec{F}_{friction}$ is the total frictional force, $\vec{M}_{pressure}$ is the axial torque (or moment) exerted by the pressure forces, and $\vec{M}_{friction}$ is the axial torque (or moment) exerted by the frictional forces on the rotor, where all quantities are computed and summed on all rotor faces (or any arbitrary patch).

p is the static pressure on the faces and \vec{X}_{face} is the position vector, from the center of rotation and ending at the face center. \vec{A}_{face} is the normal area vector of each boundary face and $\tau_{viscous}$ is the viscous stress tensor.

Appendix B

Test Cases and Validation

B.1 Turbulence Model Validation Test Case

To make sure that the turbulence models in OpenFOAM correctly predict the important flow characteristics, such as boundary layer build up near the walls and recirculation in separation zones, they have been validated using experimental data. The backward facing step case, studied by Fessler et. al. [18] was chosen as a relevant case. The computational mesh was made using the OpenFOAM built-in mesh generator, `blockMesh`, following the geometry in Figure B.1.



Figure B.1: Backward-facing step geometry. Here $h = 40\text{mm}$ and $H = 26.7\text{mm}$

The inlet velocity $U_{in} = 9.3(\text{m/s})$ gives a fully developed flow at the middle of the inlet channel (at $\sim 30h$ from the inlet), with a centerline velocity of 10.5 (m/s). This corresponds to a Reynolds number of about 1.3×10^4 , based on the half channel height.

B.2 Case specifications

Almost all turbulence models described in Appendix A have been tested on the backward-facing step case. Different turbulence models and numerical schemes as well as a set of different grids have been tested, as shown in Table B.1. The aim of the study was to compare the performance of different turbulence models to select the most suitable ones. Also, a few different numerical schemes were tested on the kEpsilon model to examine its sensitivity to the numerical schemes. Finally, a grid study was performed on three turbulence models, kEpsilon, kOmegaSST and LaunderSharmaKE models to verify how grid-dependent the models are. It should be noted that despite similar geometries, the meshes are not similar in all cases. While the kEpsilon, realizableKE, RNGkEpsilon, NonlinearKEShah, SpalartAllmaras, UD-kEpsilon, CDkEpsilon and UDTurbulencekEpsilon cases share the same meshes, the other cases have different meshes to get y^+ values in the correct range. There is no y^+ value reported for the SpalartAllmaras case, since it is not reported by the code.

Case name	Turbulence model	Convection scheme		Average y_+
		Velocity	Turbulence	
kEpsilon	$k - \varepsilon$	Gamma	Gamma	≈ 61
RNGkEpsilon	RNG $k - \varepsilon$	Gamma	Gamma	≈ 61
realizableKE	realizable $k - \varepsilon$	Gamma	Gamma	≈ 61
kOmegaSST	$k - \omega$ SST	Gamma	Gamma	≈ 61
LienCubicKE	Lien-Cubic $k - \varepsilon$	Gamma	Gamma	≈ 67
NonlinearKEShih	Non-Linear Shih $k - \varepsilon$	Gamma	Gamma	≈ 67
LRR	Launder-Reece-Rodi RSTM	Gamma	Gamma	≈ 65
LaunderGibsonRSTM	Launder-Gibson RSTM	Gamma	Gamma	≈ 61
LaunderSharmaKE	Launder-Sharma $k - \varepsilon$	Gamma	Upwind	≈ 3
LamBremhorstKE	Lam-Bremhorst $k - \varepsilon$	Gamma	Gamma	≈ 6
SpalartAllmaras	Spalart-Allmaras	Gamma	Gamma	[—]
CDkEpsilon	$k - \varepsilon$	Central	Gamma	≈ 61
UDkEpsilon	$k - \varepsilon$	Upwind	Gamma	≈ 61
UDturbulencekEpsilon	$k - \varepsilon$	Gamma	Upwind	≈ 61
lowy+kEpsilon	$k - \varepsilon$	Gamma	Gamma	≈ 26
highy+kEpsilon	$k - \varepsilon$	Gamma	Gamma	≈ 122
lowy+kOmegaSST	$k - \omega$ SST	Gamma	Gamma	≈ 26
highy+kOmegaSST	$k - \omega$ SST	Gamma	Gamma	≈ 122
lowy+LaunderSharmaKE	Launder-Sharma $k - \varepsilon$	Gamma	Upwind	≈ 1
highy+LaunderSharmaKE	Launder-Sharma $k - \varepsilon$	Gamma	Upwind	≈ 10

Table B.1: Case specifications

B.3 Results

The results are validated and analyzed with respect to normalized velocity profiles, U/U_{cl} , turbulent kinetic energy, k , wall shear stress, τ_{wall} and y^+ values respectively.

B.3.1 Normalized velocity profiles, U/U_{cl}

The velocity profiles at different sections are divided by the centerline velocity, U_{cl} , and the results have been compared to each other and experimental data. Figures B.2 and B.3 show the results for different run setups.

As the results suggest, the best prediction of the normalized velocity profiles by the high Reynolds number models is provided by the RNGkEpsilon model. The worst results are found by the Nonlinear-KEShih and LienCubicKE models. The other high Reynolds number models, including kOmegaSST, show a relatively good correspondance with the experimental data. The Reynolds stress models generally show a good accuracy. Among the low-Re models, the LaunderSharmaKE model shows the best consistency with the experimental data, compared to the LamBremhorstKE model which does not seem to give acceptable results in spite of acceptable y^+ values. Different convection schemes for the velocity and turbulence show a negligible difference in the profiles. A grid study has been performed on two high-Re models, namely kEpsilon and kOmegaSST models. kOmegaSST models yields impaired results with a too fine grid (y^+ value less than 30). The kEpsilon model, however, proves not to be affected by the grid resolution changes. The LaunderSharmaKE model is unaffected by the y^+ range tested in this study. However, the y^+ values should be kept below 11 to make sure that the model works properly. Higher y^+ values lead to very impaired results for this model.

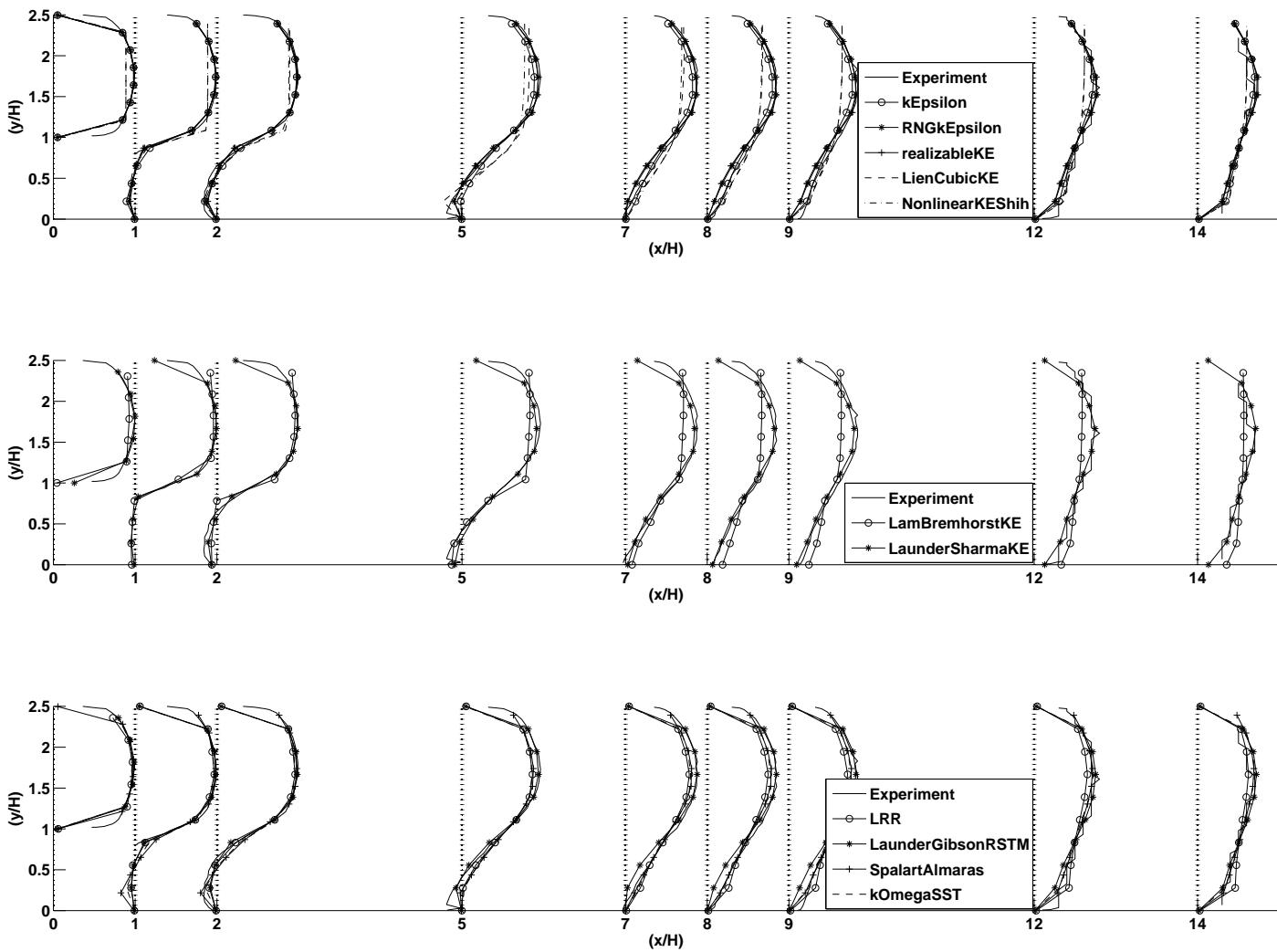


Figure B.2: Velocity profiles at different sections. Top: High-Re $k - \varepsilon$ turbulence models. Middle: Low-Re $k - \varepsilon$ Turbulence models. Bottom: Other turbulence models

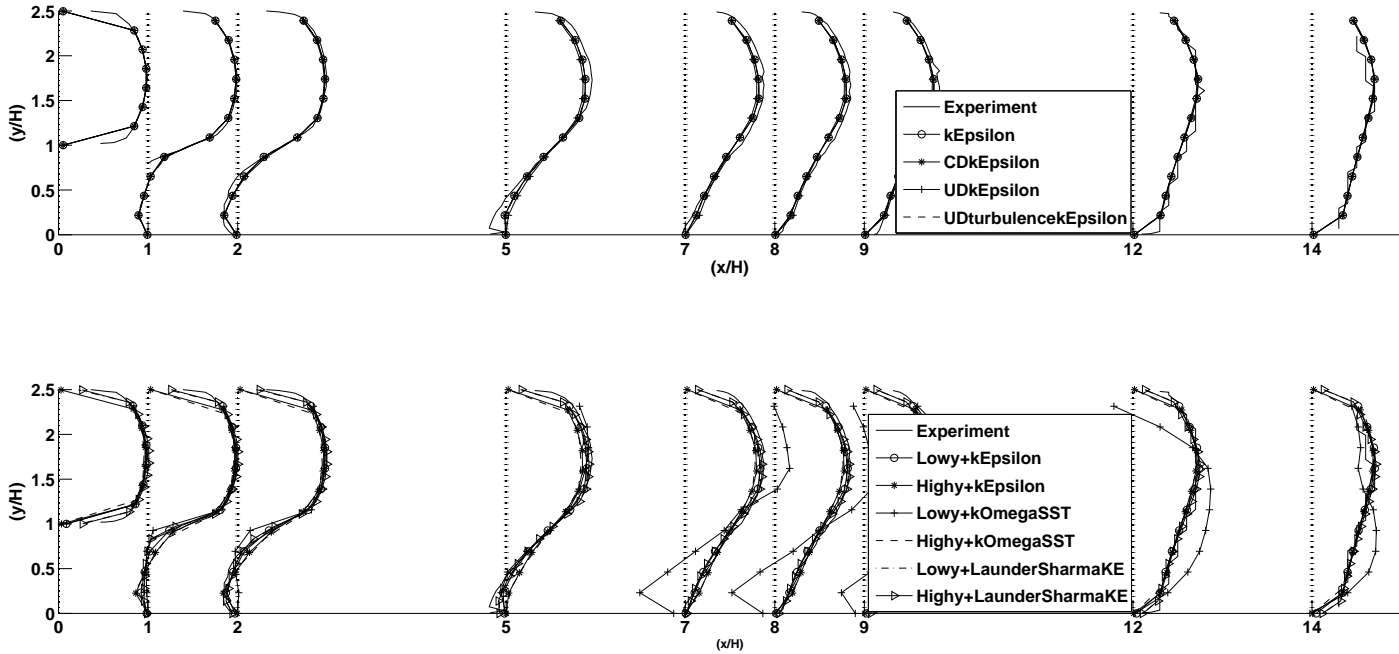


Figure B.3: Velocity profiles at different sections. Top: $k - \varepsilon$ with Different numerical schemes. Bottom: Different mesh resolutions.

B.3.2 Turbulent kinetic energy, k

The turbulent kinetic energy is computed at different sections and compared to the experimental results in Figures B.4 and B.5. Note that in the experimental results the w' component of the velocity has been assumed to be of the same order of magnitude as the v' component. The turbulent kinetic energy is then computed through

$$k = \sqrt{u'^2 + v'^2 + w'^2}$$

An investigation of the results for the turbulent kinetic energy, k , shows that all high-Re models perform rather well even in the recirculation region. The RNGkEpsilon model shows the best consistency with the experiments while again the NonlinearKEShah and LienCubicKE models give the worst results. The LaunderSharmaKE low-Re model gives almost the same accuracy as the high Reynolds number models while the results of the LamBremhorstKE model do not agree at all with the experiments. In the recirculation region, the best numerical scheme for the kEpsilon model is the upwind velocity and the Gamma turbulence. This is probably a coincidence, since it has been shown in many studies that second-order schemes are required to get good results in complex flows. Finally, the grid dependency test suggests that the kEpsilon and LaunderSharmaKE models show very alike results within the range of tested y^+ values, while the kOmegaSST model shows stronger grid-dependent characteristics. The k values for the SpalartAllmaras model have not been shown, since the model does not compute turbulent kinetic energy.

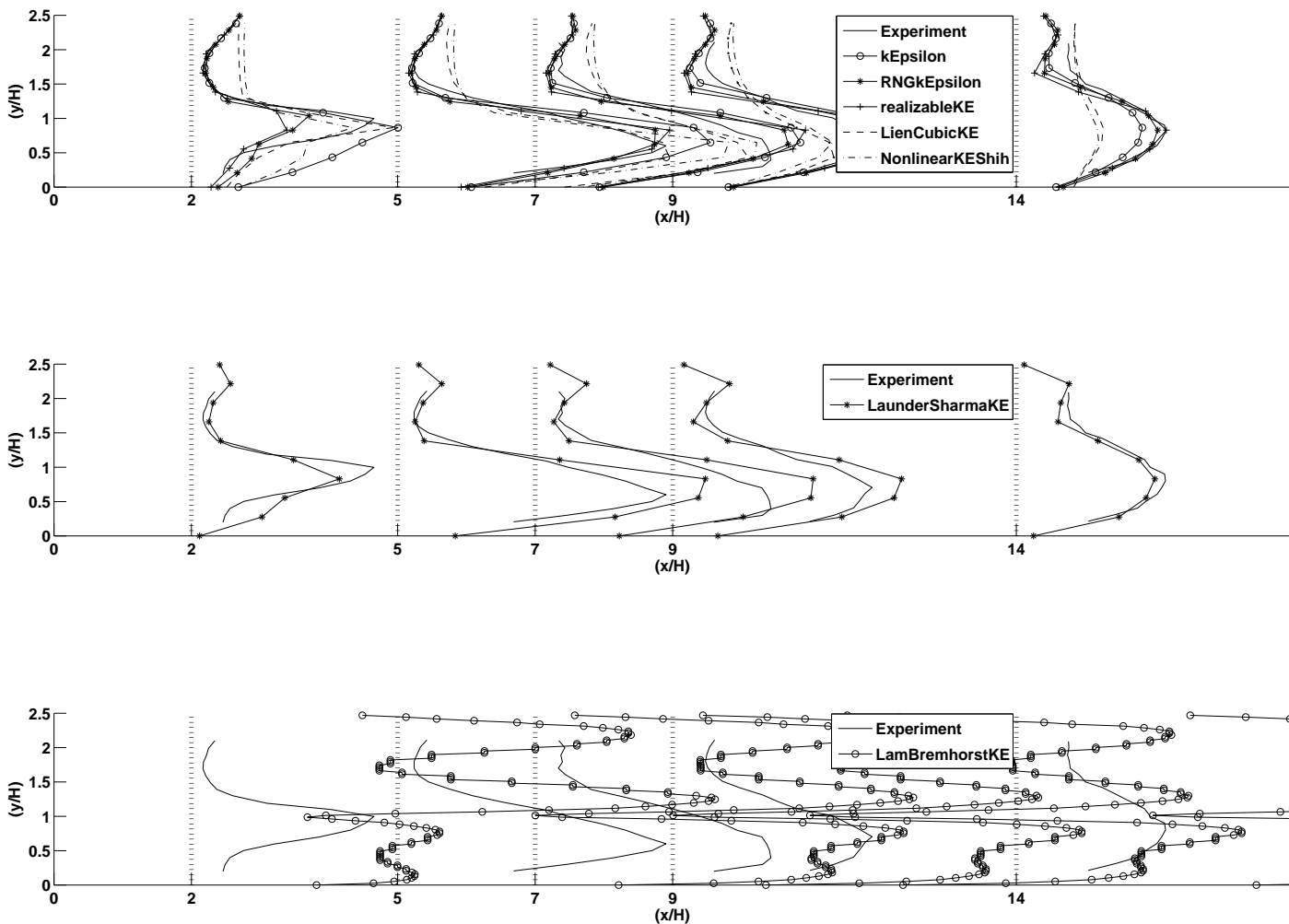


Figure B.4: Turbulent kinetic energy at different sections. Top: High-Re $k - \varepsilon$ turbulence models. Middle: Low-Re LaunderSharmaKE model. Bottom: Low-Re LamBremhorstKE model

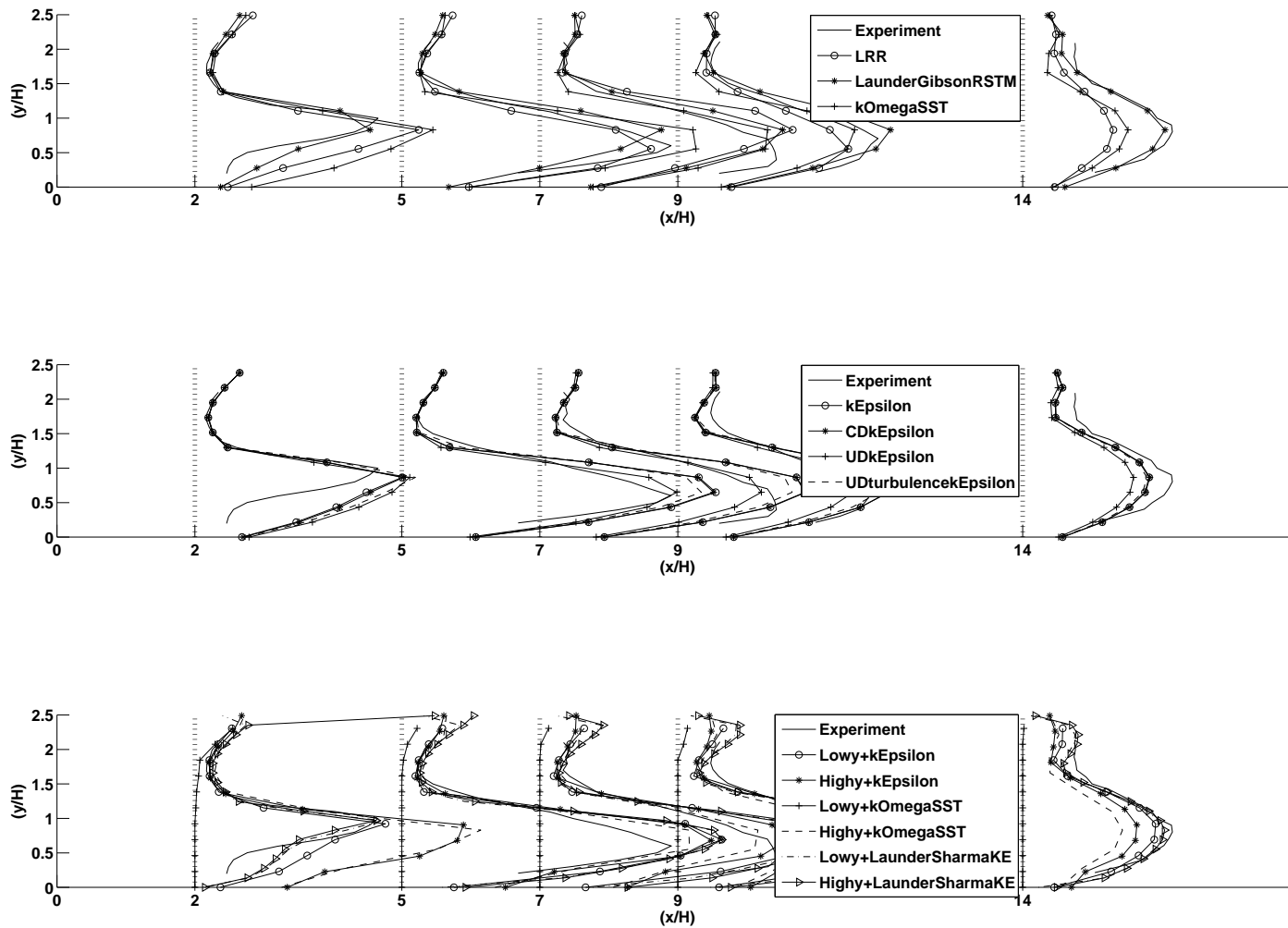


Figure B.5: Turbulent kinetic energy at different sections. Top: Other turbulence models. Middle: $k - \varepsilon$ with Different numerical schemes. Bottom: Different mesh resolutions.

B.3.3 y^+ value

Figures B.7 and B.7 show the distribution of y^+ values for all cases. The $k-\varepsilon$ models, other than NonlinearKEShih and LienCubicKE, show more or less exactly the same y^+ values. The choice of different numerical schemes for the solvers does not have a noticeable impact on the y^+ values for the same grid. The last figure in this set shows the y^+ values for the grid tests. The local y^+ values are generally not in the recommended range, which together with velocity distributions, turbulent kinetic energy and wall shear stress distributions gives a measure on how sensitive each model is to the grid resolution.

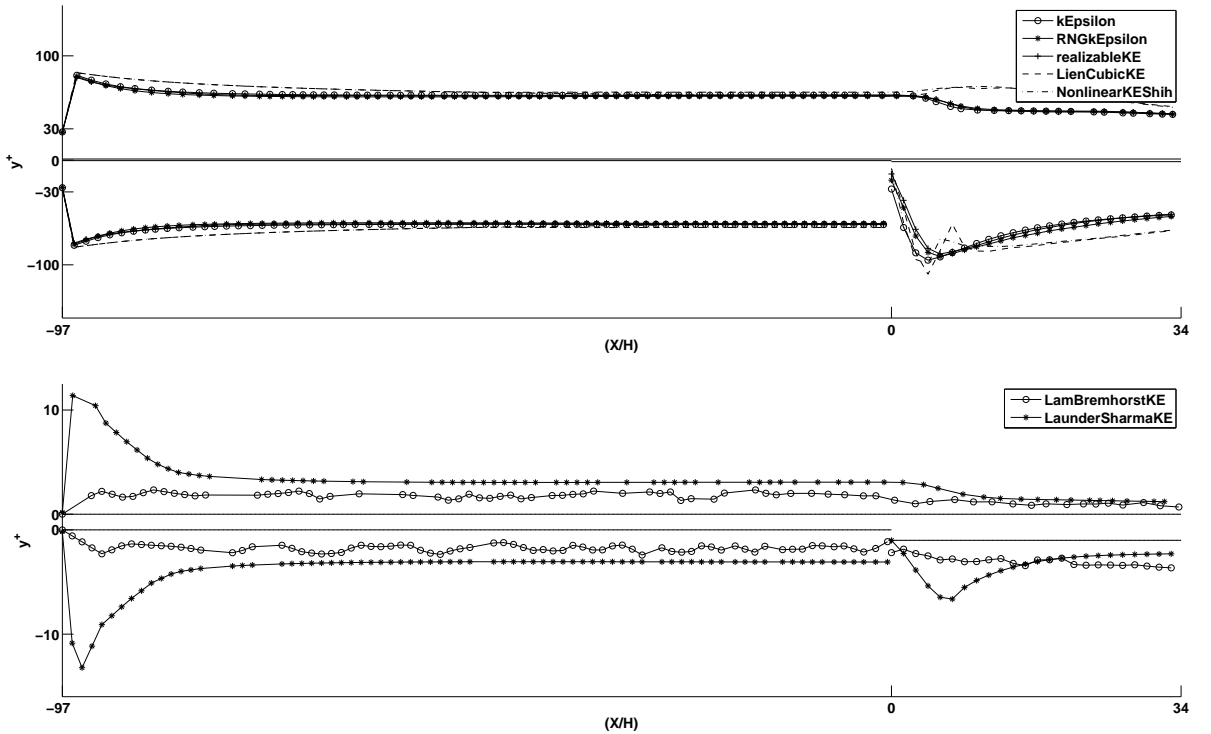


Figure B.6: y^+ distribution on the walls. Top: High-Re $k - \varepsilon$ turbulence models. Middle: Low-Re $k - \varepsilon$ Turbulence models.

APPENDIX B. TEST CASES AND VALIDATION

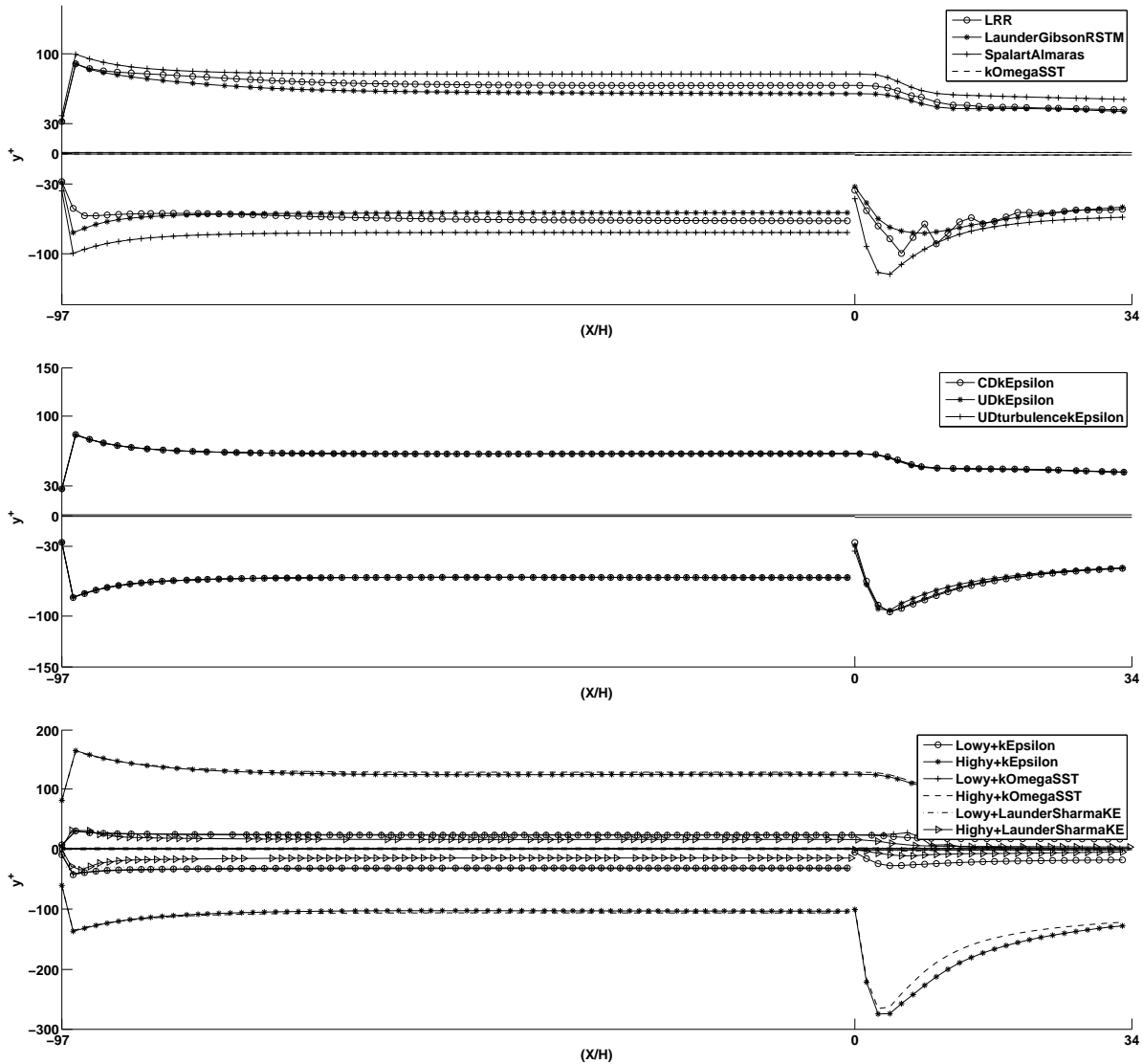


Figure B.7: y^+ distribution on the walls. Top: Other turbulence models. Middle: $k - \varepsilon$ with Different numerical schemes. Bottom: Different mesh resolutions.

B.3.4 Wall Shear Stress, τ_{wall}

Figures B.8, B.9and B.10 show the distribution of the shear stress on the walls. A comparison of different models show that except Non-linearKEShih, LienCubicKE, LamBremhorstKE and LRR, other turbulence models show more or less the same values for the wall shear stress. It should, however, be noted that the SpalartAllmaras model gives slightly higher values than the other models. Experimentally measured shear stresses at the wall are not available but are needed to validate the computational results. The results also suggest that the choice of different numerical schemes and grid resolution (except for the Lowy⁺kOmegaSST model) does not affect the simulation results of τ_{wall} considerably.

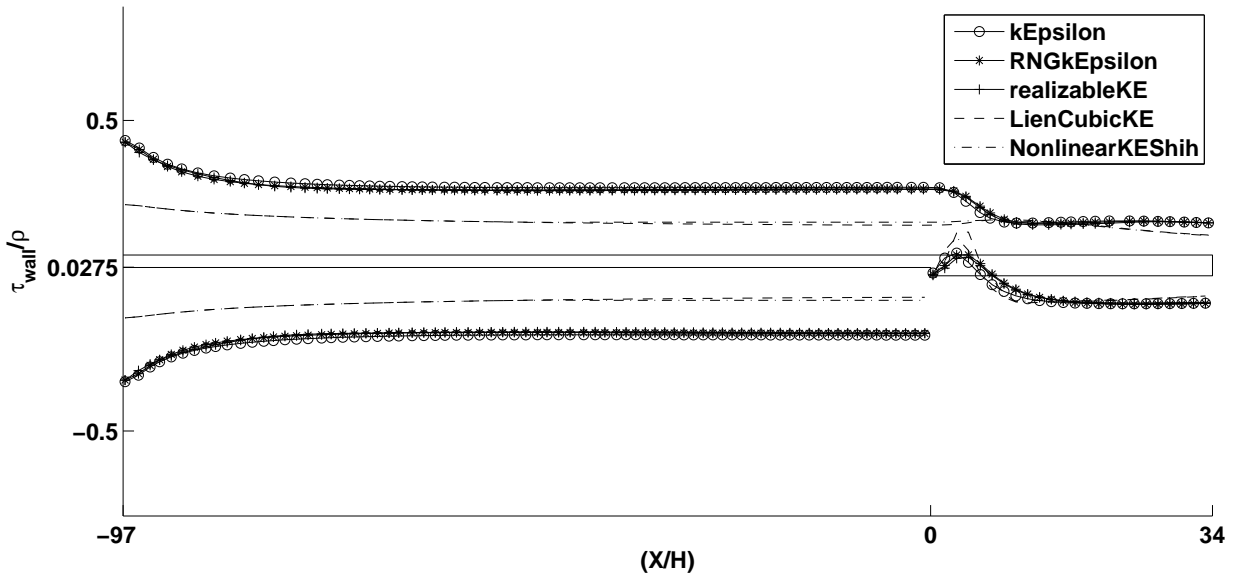


Figure B.8: τ_{wall} distributions: High-Re $k - \varepsilon$ turbulence models.

APPENDIX B. TEST CASES AND VALIDATION

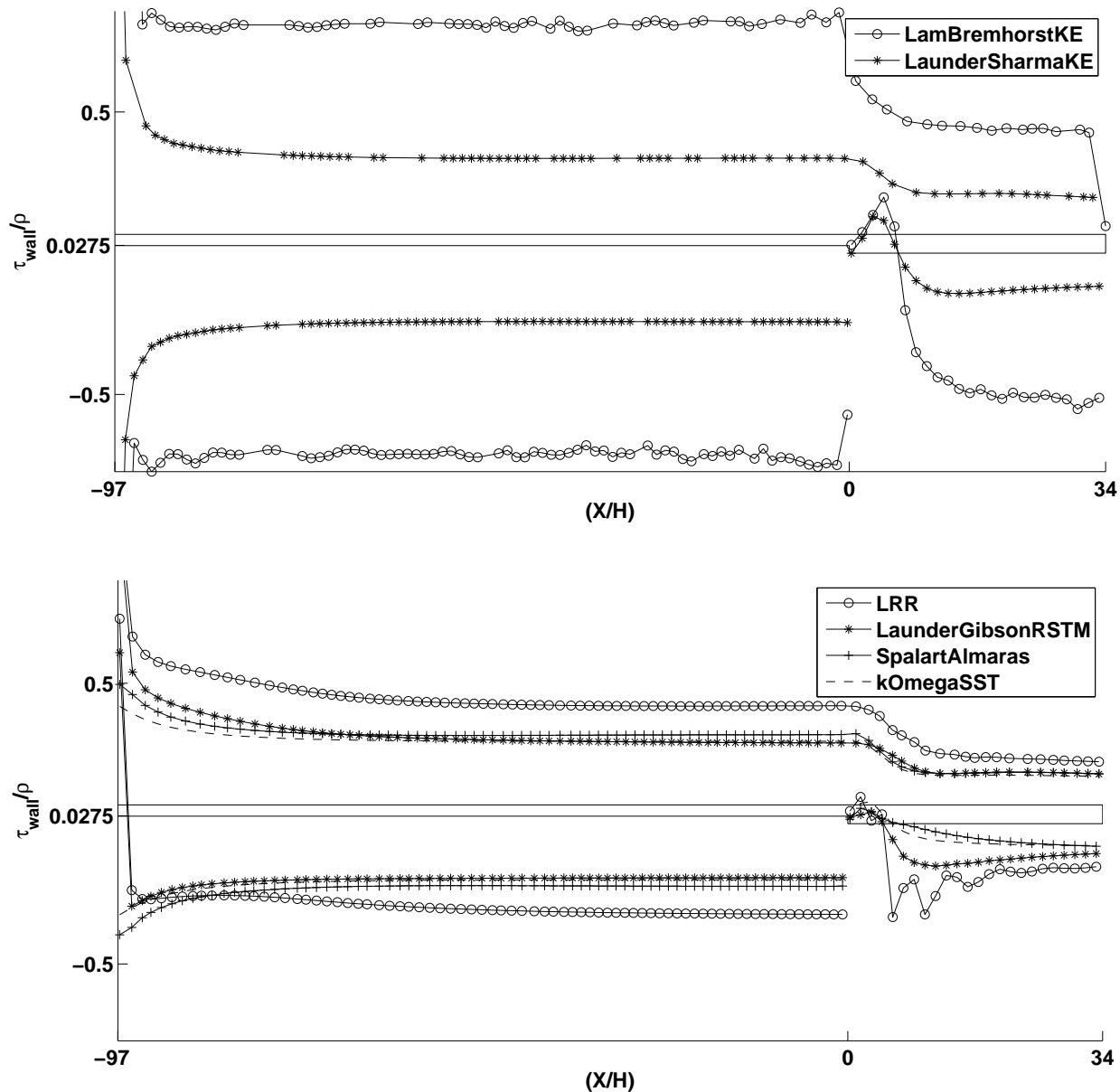


Figure B.9: τ_{wall} distributions. Top: Low-Re $k-\varepsilon$ Turbulence models. Bottom: Other high-Re turbulence models.

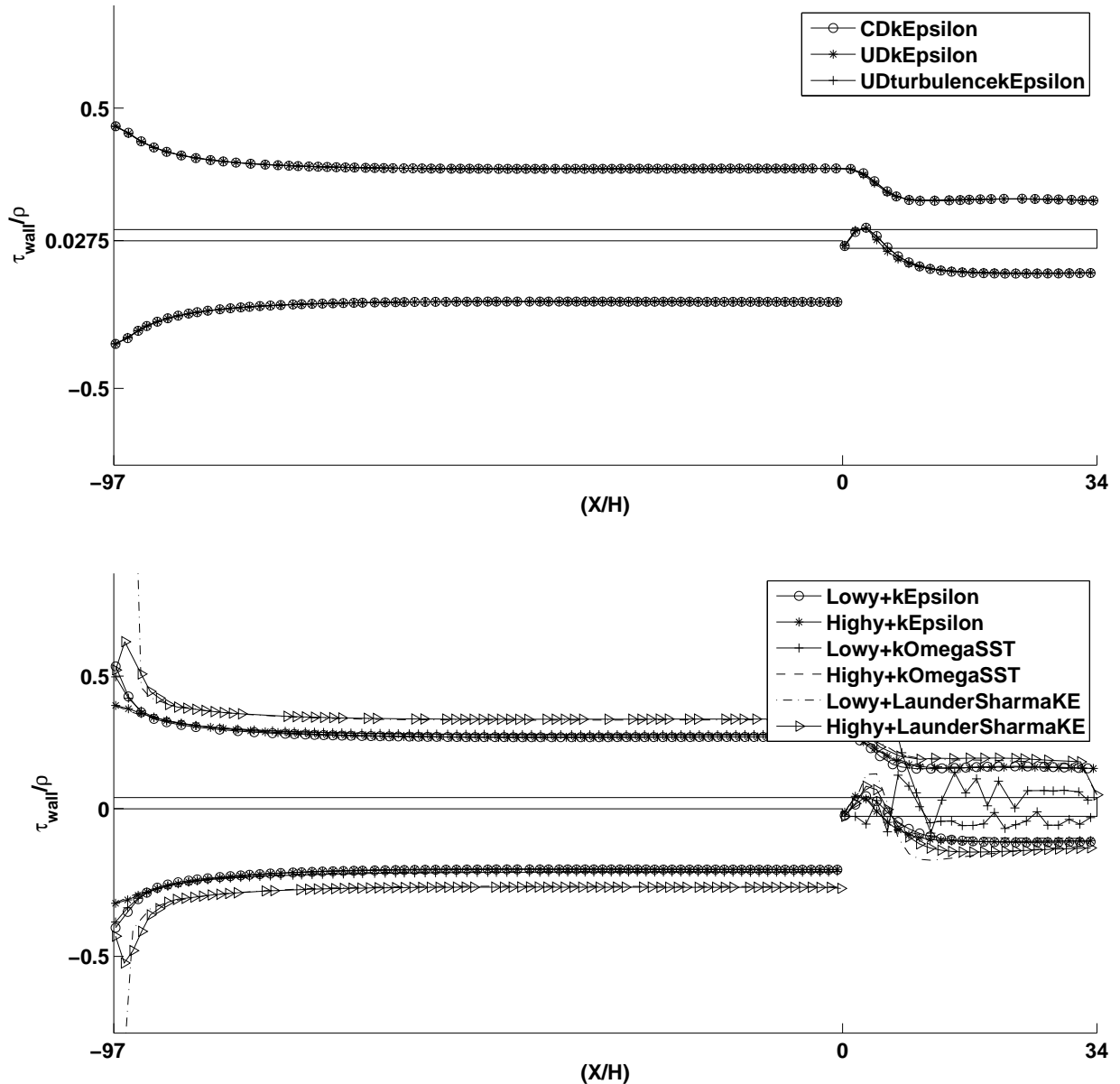


Figure B.10: τ_{wall} distributions. Top: $k - \varepsilon$ with Different numerical schemes.
Bottom: Different mesh resolutions.

B.3.5 Choice of Turbulence Model for the Generator

An important region in the backward facing step case is the recirculation region after the step. This region is particularly of high interest in this work since there are many similar separations present in generators. As it is apparent from the figures, the results of the RNGkEpsilon and LaunderSharmaKE models are very well consistent with the experimental results. However, the small height of the stator channels does not allow the use of a wall function mesh and utilization of a high-Re turbulence model within an acceptable y^+ range. This would lead to a very coarse grid in the channels, with only two cell layers in the vertical direction, and would impair the quality of the results. Therefore, the RNGkEpsilon model was not appropriate to use in the generator cases and instead, the LaunderSharmaKE model was chosen to perform the computations.

B.4 Concentric Cylinders

The flow in the generator is driven by the pressure build-up due to the rotation of the air in the space between the rotor poles and the stator. To verify that OpenFOAM is able to predict this behaviour correctly, a laminar Couette flow [19] test case has been studied. The test case consists of two concentric, infinitely long cylinders where the inner cylinder rotates and the outer cylinder is at rest. This creates a laminar flow in the space between the cylinders. The analytical pressure distribution between the inner radius, r_i , and the outer radius, r_o is given by

$$p(r) = p(r_i) + \frac{\rho \Omega_i^2 r_i^4}{(r_o^2 - r_i^2)^2} \left[\frac{-r_o^4}{2} \frac{1}{r^2} - 2r_o^2 \ln\left(\frac{r}{r_i}\right) + \frac{r^2}{2} + \frac{r_o^4 - r_i^4}{2r_i^2} \right]$$

The corresponding theoretical velocity distribution reads

$$V_\theta(r) = \Omega_i r_i \frac{\left(\frac{r_o}{r} - \frac{r}{r_o}\right)}{\left(\frac{r_o}{r_i} - \frac{r_i}{r_o}\right)}$$

Here Ω_i is the rotational speed of the inner cylinder. Figure B.11 shows that the numerical pressure and velocity distributions coincide well with their corresponding analytical solutions.

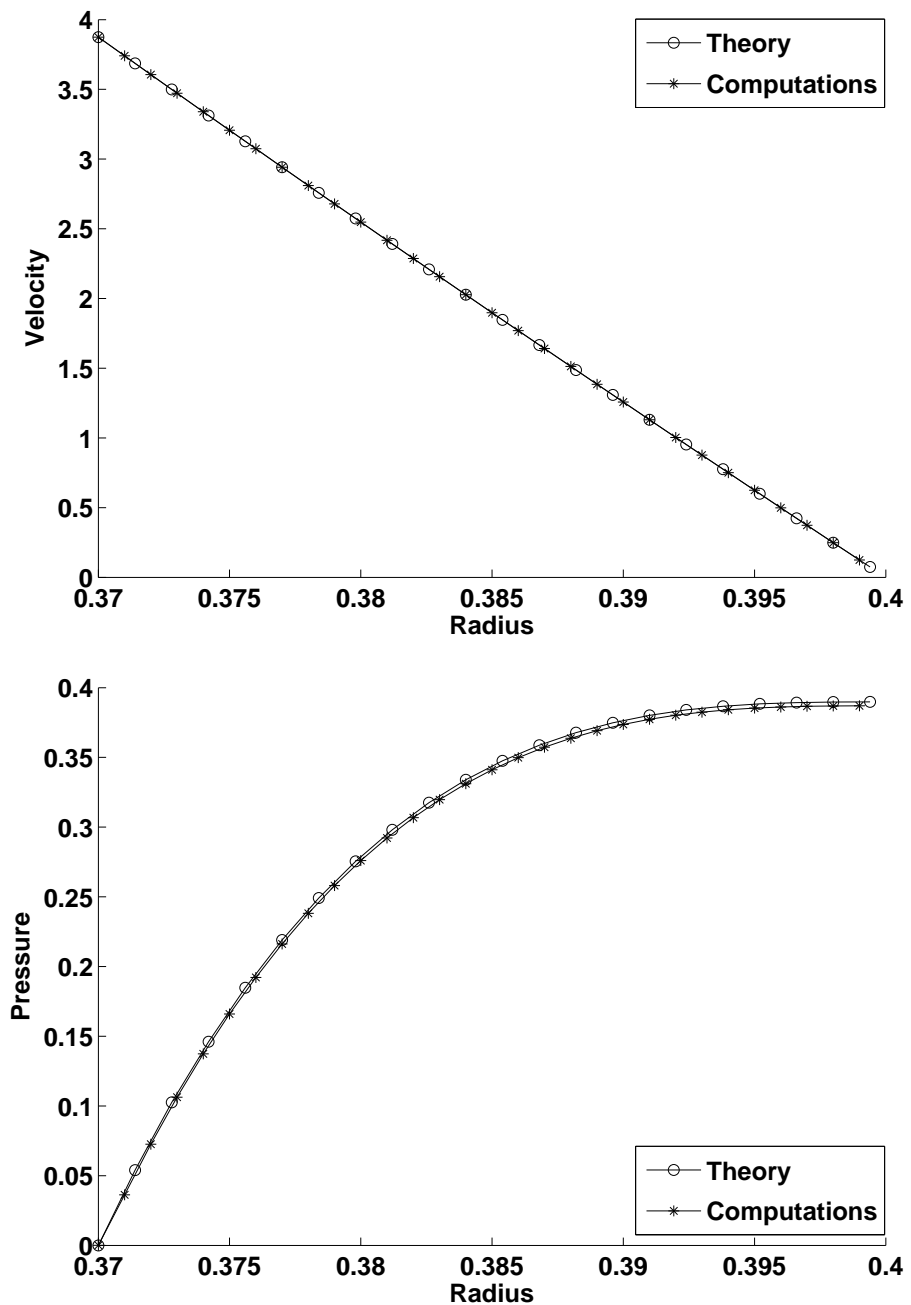


Figure B.11: Comparison of the numerical and theoretical velocity (Top) and pressure (Bottom) distributions for the laminar Couette flow.

Bibliography

- [1] H.K. Versteeg and W. Malalasekera. *An Introduction to Computational Fluid Dynamics: The Finite Volume Method*. Addison-Wesley, 2nd edition, 2007. ISBN-10: 0131274988.
- [2] F.S. Lien and M.A. Leschziner. Computational modelling of 3d turbulent flow in s-diffuser and transition ducts. *Engineering Turbulence Modelling and Measurements*, 2:217–228, 1993.
- [3] V. Yakhot and S.A. Orszag. Computational modelling of 3d turbulent flow in s-diffuser and transition ducts. *Physics of Fluids A*, 4:1510–1520, 1992.
- [4] F.S. Lien and M.A. Leschziner. A new $k-\varepsilon$ eddy viscosity model for high reynolds number turbulent flows. *Computers Fluids*, 24:227–238, 1995.
- [5] F. Menter and T. Esch. Elements of industrial heat transfer predictions. In *16th Brazilian Congress of Mechanical Engineering*, COBEM, 2001.
- [6] J. Zhu and T.H. Shih. Computation of confined coflow jets with three turbulence models. *International Journal of Numerical Methods in Fluids*, 19:939–956, 1994.
- [7] F.S. Lien, W.L. Chen, and M.A. Leschziner. Low-reynolds-number eddy-viscosity modelling based on non-linear stress-strain/vorticity relations. *Engineering Turbulence Modelling and Experiments*, 3:91–100, 1996.
- [8] A.A Dafa'alla, E. Juntasaro, and M.M. Gibson. Computational of periodic turbulent boundary layers with moderate adverse pressure gradient. *International Journal of Heat and Fluid Flow*, 18:443–451, 1997.
- [9] M. Raissee. Recent progress in prediction of complex turbulent flows using a cubic nonlinear eddy-viscosity model. *Physica Scripta*, T132(014004).

- [10] K.P. Jha and S.K. Dash. Implyoment of different turbulence models to design of optimum steel flows in a tundish. *International Journal of Numerical Methods in Heat and Fluid Flow*, 14(8).
- [11] F.S. Lien and M.A. Leschziner. Modelling 2d separation from high-lift aerofoil with non-linear eddy-viscosity model and second-moment closure. *Aeronautical Journal*, 99:125–144, 1995.
- [12] F.S. Lien, W.L. Chen, and M.A. Leschziner. Low-reynolds-number eddy-viscosity modelling based on non-linear stress-strain/vorticity relations. *Engineering Turbulence Modelling and Experiments*, 3:91–100, 1996.
- [13] B.E. Launder, G.J. Reece, and W.Rodi. Progress in the development of a reynolds-stress turbulence closure. *Journal of Fluid Mechanics*, 68(3).
- [14] F.S. Lien and M.A. Leschziner. Assessment of turbulence-transport models including non-linear rng eddy-viscosity formulation and second-moment closure for flow over a backward-facing step. *Computers Fluids*, 23(8).
- [15] C.L. Rumsey, D.O. Allison, R.T. Biedron, P.G. Buning, T.G. Gainer, J.H. Morrison, S.M. Rivers, S.J. Mysko, and D.P. Witkowski. Cfd sensitivity analysis of a modern civil transport near buffet-onset conditions. NASA/TM-2001-211263, 2001.
- [16] H. Jasak, H.G. Weller, and A.D. Gosman. High resolution nvd differencing scheme for arbitrary unstructured meshes. *International Journal for Numerical Methods in Fluids*, 31:431–449, 1999.
- [17] O. Petit, M. Page, M. Beaudoin, and H.Nilsson. The ercoftac centrifugal pump openfoam case-study. In *International Meeting of the Workgroup on Cavitation and Dynamic Problems in Hydraulic Machinery and Systems*, 2009.
- [18] J. Fessler and J. Eaton. Turbulent modification by particles in a backward-facing step flow. *Journal of Fluid Mechanics*, 394:97–117, 1999.
- [19] F. M. White. *Fluid mechanics*. McGraw Hill, 6th edition, 2008. ISBN 978-0-07-128645-9.

Paper I